

Dynamics of Entangled Polymeric Fluids in Two-roll Mill studied via Dynamic Light Scattering and Two-color flow Birefringence. I. Steady flow

Subrata Sanyal[†], Dmitry Yavich^{*} and L. Gary Leal

Department of Chemical Engineering, University of California at Santa Barbara, Santa Barbara, CA 93106-5080, U.S.A.

(June 13, 2000)

We present the experimental results on a series of high molecular weight, entangled polystyrene solutions subjected to a “mixed” shear and elongational flow-type generated in a co-rotating two-roll mill. For steady-flows as well as for start-up of flows from rest, we used two different optical methods to study the dynamics of entangled polymeric fluids: two-color flow birefringence (TCFB) and dynamic light scattering (DLS). Using the TCFB method, we measured the birefringence, Δn , and the orientation angle, χ , of the optic axes in the solution and thereby the generalized viscosity function, η (with the use of stress-optical relations). The DLS method was applied to measure the velocity-gradient, $\dot{\gamma}$, and the flow-type parameter λ for the polymer solutions under flow conditions identical to the TCFB measurements. For low deformation rates the symmetry of the flow-field was reduced with the use of polymeric fluids compared to that seen with a Newtonian fluid. A molecular constitutive Doi-Edwards-Marrucci-Grizzuti (DEMG) model which includes polymer chain-stretching effects, has been used to numerically simulate the predictions for Δn , χ , and η under steady flow conditions for the polystyrene fluids with $\dot{\gamma}$ and λ , measured via DLS, as inputs to the model. A detailed comparison of the DEMG model predictions with the experimental results shows that the model works qualitatively as well as quantitatively for the low and intermediate deformation rates, but fails at high rates of deformation by predicting a stronger chain-stretching than observed experimentally. The effect of polymer molecular-weight and number of entanglements per chain are highlighted.

I. INTRODUCTION

The majority of prior experimental studies of the dynamics of polymeric fluids were based on the simple shear flow. The main advantage is that the complete kinematics of these homogeneous flow-fields is known a priori, and experimental measurements of velocity-gradients are not necessary. On the other hand, the majority of the polymer processing applications employ flows that are inhomogeneous and often involve a mixture of simple shear and pure extension. This have provided one motivation for recent experimental as well as theoretical studies of the behavior of the polymeric fluids in “mixed” or purely extensional flows (also called the “strong” flows [1], which in two-dimensions would require the magnitude of the strain-rate to exceed the vorticity). Generally, such strong flows appear only as a local part of some otherwise globally inhomogeneous and “weak” [1] flows. Examples of such flows include the stagnation zone in a cross-slot or cross-jet device; the converging zone of a contracting channel; and the stagnation region in two- or four-roll mills. The velocity-field in these local region for any polymeric fluid will be very different from that of a Newtonian fluid of similar density and viscosity, because the flows are globally inhomogeneous and the fluid’s viscoelastic nature. It is therefore insufficient to measure only the birefringence (or stress in a rheological experiment), without simultaneously measuring the velocity-gradient field by some technique.

Different indirect techniques, e.g., Particle Imaging Velocimetry and Laser Doppler Velocimetry [2], hot wire

anemometers [3], forced Rayleigh scattering [4], holographic grating methods [5], etc. have been employed in the past for the measurement of velocity-gradients in time varying flows, but each exhibits some characteristic drawbacks. Provided that the flow is laminar and nonchaotic, the dynamic light scattering (DLS) technique [6,7] is one extremely valuable method for the *direct* measurement of velocity-gradients in strong flows. The high degree of spatial resolution of the laser light as well as the very high temporal resolution of the present day correlators has made it possible to use DLS for precise determination of velocity-gradients for both steady and time-dependent flows even in very small-scale flow systems with velocity-gradients that change relatively in time. Further, unlike other methods mentioned above, DLS is nonintrusive in nature.

The most frequently used indirect rheo-optical probe of polymer conformation in two-dimensional flows has been the flow birefringence technique [8]. Since it provides an average measure across the flow in third direction, it is only approximately *local* in that sense. Early studies using traditional flow birefringence technique were primarily restricted to steady flows. On the other hand, recent studies [9–13] for both dilute and concentrated polymer solutions in time-dependent flows have used two-color flow birefringence (TCFB) [14] and/or phase-modulated birefringence [15] techniques to simultaneously measure the retardance (and hence the birefringence, Δn) and the orientation angle, χ , of the principle axis of the refractive-index tensor with respect to the axes fixed on the flow-cell, in a single experiment.

The theoretical understanding of the dynamics of entangled polymer solution and melts is far from complete. Using de Gennes' [16] original idea of "reptation", Doi and Edwards (DE) proposed a tube model [17], which views the polymer chain as a sequence of segments confined in a tube-like region. The tube is defined by the topological constraints on the lateral motion and orientation imposed by neighboring chains. The segmental stretching can relax on a timescale similar to that for an unconstrained chain (dilute systems), i.e., the Rouse time τ_R , and the segmental orientations can only relax via reptational dynamics i.e., through longitudinal diffusion to escape the tube which requires a much longer timescale τ_d , called the reptation or disengagement time. These two time scales are related via N_e , the number of entanglement points per chain: $\tau_d = 3N_e\tau_R$. The DE model is expected to be valid for highly entangled ($N_e \gg 1$) polymeric samples. Thus the original DE model neglects the chain-stretching effects by assuming that the "snap-back" of the stretched chain to its equilibrium length is instantaneous (i.e., $\tau_R \ll \tau_d$) and develops constitutive equations which incorporate segmental orientational dynamics only. This simplified model has been quite successful in many rheometric flows such as steady simple shear and oscillatory shear, where chain-stretching is expected to be insignificant. On the other hand, serious inherent limitations of DE theory have long been recognized for the case of strong, extension-dominated flows [9–13,18] and also in transient shear flows, where chain-stretching is important. Over the past decade, this model has seen several improvements to include chain-stretching in the uniform [11,19], non-uniform [20,21] and finitely-extensible [22] form. The predictions of the resulting so-called Doi-Edwards-Marrucci-Grizzuti (DEMG) model has been studied in detail in a recent set of papers by Mead *et al.* [23,24].

The aim of the present paper is to understand the dynamics of entangled, high molecular weight polymeric fluids subjected to the strong, extension-dominated flows (i.e., for strong two-dimensional flows in the sense of Astarita [1]). To this end, we present two-color flow birefringence and dynamic light scattering results for a series of entangled polystyrene solutions in steady, near-homogeneous, planar flows created by a co-rotating two-roll mill. A detailed comparison of the experimental results for birefringence, orientation angle and generalized extensional viscosity (defined below, and obtained via stress-optical relation) for the three entangled samples to the predictions from the numerical simulation of the DEMG model [23] is carried out using the measured flow data as input to the model. The effect of molecular weight and number of entanglements per chain of the polymers on the results are demonstrated.

In sec. II we provide the necessary details related to our experiments, namely, the samples we used (sec. II.A); the linear viscoelastic measurements (sec. II.B); and the

experimental apparatus (sec. II.C). The two-color flow birefringence and the dynamic light scattering techniques and apparatus involved are described in brief along with the two-roll mill flow-cell in sec. II.C. Section III deals with the results of the steady-state flow experiments (sec. III.A) using the DLS method and comparison of the steady flow TCFB results with the DEMG model (sec. III.B). Finally, sec. IV contains a summary of our findings and conclusion.

II. EXPERIMENTAL DETAILS

A. Materials

The Newtonian fluid sample used was a suspension of spherical polystyrene particles (polyballs) of diameter $0.11\mu\text{m}$ (Polysciences Inc., U.S.A.) in glycerol (Sigma Chemical Co., U.S.A., ACS Reagent) at a concentration of 150 ppm. As shown in Table I, three non-Newtonian fluids, named PS81, PS82 and PS2, were made using two standard, fairly monodisperse polystyrene samples (Tosoh Co., Japan), namely $M_w = 8.42 \times 10^6$, $M_w/M_n = 1.17$, Lot. No. TS-31 for one and $M_w = 2.89 \times 10^6$, $M_w/M_n = 1.09$, Lot. No. TS-10 for the other. Here M_w and M_n specify the weight-average and the number-average molecular weights respectively. The solvents were prepared by adding polystyrene oligomer with $M_w = 6000$ or 2500 and a broad molecular weight distribution to toluene (Aldrich Chemical Co., Inc., U.S.A., ACS spectrophotometric grade) at mixing ratios by weight (toluene: 2500 PS = 43:57 for PS81 and PS82, and 48:52 for PS2), and allowing the mixture to dissolve at room temperature ($= 20^\circ\text{C}$) for a few days with occasional slow mixing using a magnetic stirrer. Measured amounts of high molecular weight polystyrene samples were then added to these oligomer solvents to achieve the desired concentrations, c , shown in Table I. The complete solution was then thoroughly mixed in a glass bottle for several hours by continuously rolling the bottle on its side in a Rollacell (New Brunswick Scientific Co., Inc., U.S.A.). In order to reduce the background scattering in the light scattering experiments, the samples were filtered using Milipore filters with $5\mu\text{m}$ pore size for the polymer solutions and $0.45\mu\text{m}$ pore size for the polyball suspension.

The flow-cell was pre-cleaned with acetone (Fisher Scientific, U.S.A., ACS spectranalyzed), oven-dried at 50°C and brought back to the room temperature everytime before the fluid sample was transferred into the cell via an air-tight siphon system. To minimize the loss of toluene in the precess of fluid transfer, the use of an inactive gas in the siphon system was necessary. For this purpose, we used compressed nitrogen gas to maintain a minimum pressure differential in the siphon to fill up the cell volume ($\sim 100\text{ mL}$) in a couple of hours.

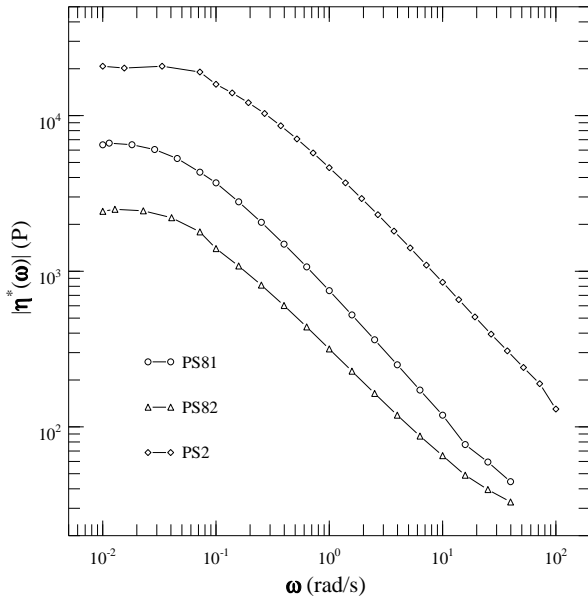


FIG. 1. The modulus of complex dynamic viscosities, $|\eta^*|$ (in P), as a function of the radial frequency, ω (in rad/s), for the three polystyrene samples, measured at 20°C.

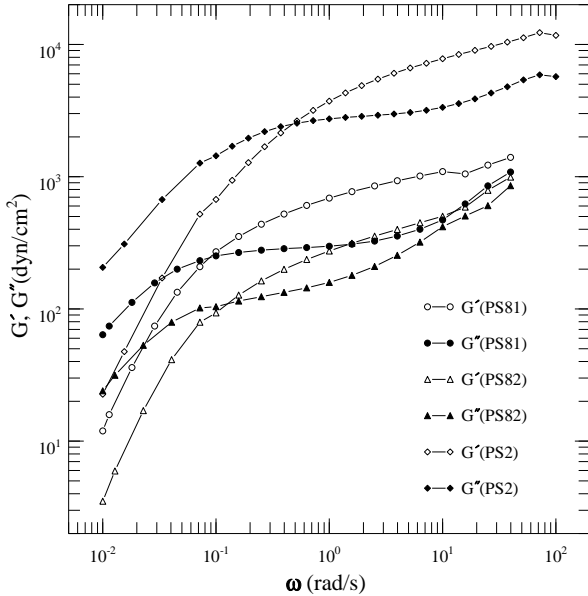


FIG. 2. The dependence of the elastic modulus, G' , and the viscous modulus, G'' , (both in the units of dyn/cm²) on angular frequency, ω (in rad/s), for the three polystyrene samples at 20°C.

B. Linear viscoelastic measurements

The linear viscoelastic shear flow properties of the three polymer solutions were measured, at a temperature of 20°C, using a Rheometrics Mechanical Spectrometer (RMS-800) in a cone-and-plate geometry with a cone diameter of 40 mm and a gap angle of 4°. The measured

moduli of complex dynamic viscosities $|\eta^*|$ of the three liquids are plotted against the angular frequency ω in Fig. 1. We note that the viscosity of PS2 is about an order of magnitude higher than the other two samples; it is a much less mobile liquid. The sample PS81 is a couple of times more viscous than PS82. The typical nature of the three curves seen in Fig. 1 is very similar, namely, $|\eta^*|$ is almost constant at low frequency $\omega \leq 3 \times 10^{-2}$ rad s⁻¹ and beyond this ω it shows a “shear” thinning behavior, following an empirical power law $|\eta^*| = K\omega^n$, over the entire experimental frequency range, with the correlation coefficient R^2 being about 0.99 or higher in all three cases. The power law constant K and the exponent n , obtained from a linear regression of the data are given in Table I. We note that although the values of K are significantly different in these samples, the slope of the complex dynamic viscosity versus angular frequency curves in a double-logarithmic plot in Fig. 1 is about same for two solutions with $N_e \sim 13$ and larger than the slope with $N_e \sim 7$.

From the low frequency Newtonian plateau of these curves, the zero “shear-rate” viscosity η_0 is extracted for these samples and is shown in Table I. The number of entanglement points per chain, N_e , can be defined by analogy with the classical theory of rubber elasticity,

$$G_N^0 = \left(\frac{cRT}{M_e} \right) \equiv \left(\frac{cRT}{M_w} \right) N_e, \quad (1)$$

where c is the polymer concentration in g cm⁻³, $M_e = M_w/N_e$ is the molecular weight between entanglements, R is the gas constant and T is the absolute temperature. We have used the approximate expression for the plateau modulus,

$$G_N^0 = 3.44 \times 10^6 \times c^{2.4} \text{ dyn/cm}^2 \quad (c \leq 0.1 \text{ g cm}^{-3}), \quad (2)$$

obtained experimentally by Osaki *et al.* [25] for polystyrene solutions in a good solvent. The values obtained using this equation agrees reasonably well with measured values. Thus Eqns. (1) and (2) leads to

$$N_e = 1.41 \times 10^{-4} \times M_w \times c^{1.4} \quad (3)$$

for our experiments and the calculated values of N_e for the polystyrene samples are shown in Table I.

The dynamic moduli of PS81, PS82 and PS2 are measured on the same rheometer RMS-800 with the same pair of cone and plate as for the data in Fig. 1 and are shown in Fig. 2. Both, the elastic modulus (G') and the viscous modulus (G'') show a strong frequency dependence for all three cases. The values of the moduli G' and G'' for PS81 is higher than that of PS82, both having an order of magnitude lower values than in the case of PS2. Each of these pair of complex moduli shows a pattern of G'' dominating over G' in the low frequency

“terminal zone” and the values of G' taking over that of G'' in the higher frequency “plateau region”, typical of polymeric fluids. In the low frequency flow region, the storage modulus G' approaches a quadratic dependence on ω and the loss modulus G'' shows a linear dependence, again a typical behavior of polymers with a narrow molecular weight distribution. At higher frequencies G' and G'' tend to converge, which may be due to the formation of transient entanglement network [26]. The value of ω at which the storage modulus falls below the loss modulus is highest in PS2 and lowest in PS81. Assuming that this crossing point frequency corresponds to the inverse of the disengagement time τ_d , we have estimated the values of τ_d to be 67.50 s, 54.18 s and 16.80 s respectively for PS81, PS82 and PS2. Using the prediction $\tau_R = \tau_d/(3N_e)$ from reptation theory [17], we have calculated the Rouse time, τ_R , for each sample as reported in Table I. To check these values, we can use the correlation of Menezes and Graessley [27]

$$\tau_R = \left[\frac{6 (M_c)_0^{a-1}}{\pi^2 \rho R T} \right] \frac{\eta_0}{M_w^{(a-2)} \nu^{(a-1)b+1}}, \quad (4)$$

where for polystyrene we use [26] $(M_c)_0 = 33,000$, $a = 3.4$, $b = 1.3$, density $\rho = 1.07 \text{ g cm}^{-3}$ and volume fraction $\nu = \rho c$. The calculated Rouse times are 1.95 s, 3.84 s and 0.87 s for PS81, PS82 and PS2 respectively. It is unclear to us why the values calculated from Eqn. (4) are not in closer agreement with those obtained here experimentally, though they are in the same ballpark. In what follows, we use the experimentally determined values listed in Table I.

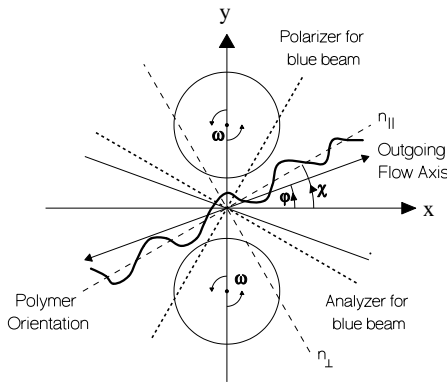


FIG. 4. Schematic representation of the light scattering configuration.

1. Two-color flow birefringence

The TCFB technique [14] simultaneously measures both retardance and orientation χ of the principal axis of the refractive-index tensor \underline{n} relative to the axes $[(x, y)]$ in Figs. 3 and 4] fixed in the flow device. The light source is an Argon-ion laser (Spectra Physics Model 2020) operating at $\sim 300 \text{ mW}$, which emits two intense wavelengths at $\lambda_B = 4880 \text{ \AA}$ (blue) and $\lambda_G = 5145 \text{ \AA}$ (green). As shown in Fig. 5, with the use of several optical elements, each of these beams (independently polarized at 45° relative to each other) are made to pass along an identical optical path through the sample in a two-roll mill which is placed between crossed polarizers. Since the flow is non-homogeneous, to ensure the collinearity of the two beams (with identical optical properties, e.g., beamwidth, Gaussian beam-profile etc.) passing through the same element of fluid in the flow-cell is very crucial in this set-up. Each of the measured intensities (at the photodetectors) depends upon the current degree of optical anisotropy of

FIG. 3. Relative orientation of the optical system including the flow-cell and the definition of the coordinate systems.

the sample in the plane of flow $[(x, y)$ plane in Fig. 3], — i.e., the birefringence, $\Delta n = n_{\parallel} - n_{\perp}$ — and χ , which provides a measure of the average orientation of Kuhn segments in the polymeric liquid. Further details of the optical system are described in Ref. [10] and will thus not be repeated here. The measured overall error due to nonidealities of the optical components indicate that the maximum extinction ratios detectable in this set up with the flow device (loaded with polymer solution), for both colors, are typically $\mathcal{O}(2 \times 10^{-5})$.

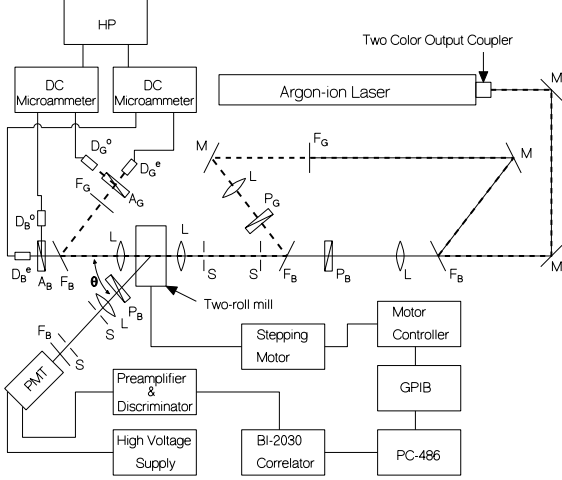


FIG. 5. Schematic showing the optical layout for the two-color flow birefringence and the dynamic light scattering setup. M: mirror; F: interference filter; L: lense; P: polarizer; A: analyzer; D: photodiode; S: pinhole; θ : scattering angle. The subscripts B & G specify the blue (continuous line) and the green (broken line) laser beams, respectively. The superscripts o and e refer to the ordinary and extraordinary beams, respectively.

2. The two-roll mill and the flow

The two-roll mill is a flow device [10] consisting of two cylinders driven simultaneously by a single DC stepping motor (Superior Electric, U.S.A., SLO-SYN motor type MO62-FD-09). The cylinders rotate at the same angular velocity and in the same direction to generate a flow between the roller pair, that can be approximated at the central stagnation point by a linear (or homogeneous), planar velocity-field of the form

$$v = \nabla \vec{v} \cdot \vec{r}. \quad (5)$$

Here, \vec{r} is the position vector defined in the flow plane w.r.t. the (x, y) frame, shown in Figs. 3 and 4. The velocity-gradient tensor $\nabla \vec{v}$ in this coordinate system is given by

$$\nabla \vec{v} = \dot{\gamma} \begin{bmatrix} \epsilon & 1 \\ \lambda & -\epsilon \end{bmatrix}, \quad 0 < \lambda \leq 1. \quad (6)$$

If we assume further that the flow is *symmetric* about the central (x, z) plane between the rollers, as in the case for a Newtonian fluid at zero Reynolds number, then

$$\epsilon \equiv 0 \quad (\text{symmetric flow}). \quad (7)$$

In that case, Eqn. (6) can be completely characterized by two scalar parameters, namely, the magnitude of the velocity-gradient $\dot{\gamma} \equiv |\nabla \vec{v}|$ (also called the “shear-rate”) and the flow-type parameter λ . The parameter λ is a measure of the ratio of strain-rate to vorticity, and is defined as,

$$\frac{\|\underline{\underline{E}}\|}{\|\underline{\underline{\Omega}}\|} = \frac{1 + \lambda}{1 - \lambda}. \quad (8)$$

Thus, $\lambda = 0$ corresponds to a simple shear flow, $\lambda = 1$ to a purely extensional (also called hyperbolic) flow, and intermediate values of λ represent a “mixed” shear and elongational flow-type (also called a “strong” or extension dominated flow [1], since the strain-rate exceeds the vorticity). In sharp contrast to other extensional flow devices, polymer molecules at the stagnation region of a two-roll mill have very long residence time and hence are subjected to very large total strains. Consequently, they can, in principle, achieve the maximum change in conformation that is consistent with a particular strain-rate [9]. For a Newtonian fluid, at very low Reynolds numbers, where the symmetric flow assumption is valid, the creeping flow solutions [9] for a two-roll mill in an unbounded fluid approximately relate the values of the corresponding velocity-gradient $\dot{\gamma}_N$ and the flow-type parameter λ_N in the stagnation region with the geometry of the cell (i.e., the roller radius R and the gapwidth $2h$), via

$$\lambda_N = \left(\frac{4 \coth K_f}{K_f} - 1 \right)^{-1}, \quad \dot{\gamma}_N = \frac{A\omega}{\lambda_N} \\ \text{with } A = \frac{K_f}{K_f + \sinh K_f \cosh K_f}, \quad (9)$$

where ω is the angular velocity of the rollers and the parameter K_f is given by

$$1 + \frac{h}{R} = \cosh K_f. \quad (10)$$

The symmetry axes of the flow-field, the principal optical axes of the solution, as well as the relative orientation of the blue polarizer and analyzer for the two-roll mill set is shown in Fig. 3. It may be noted that the Newtonian value of the flow-type parameter, λ_N , is also related to the acute angle of crossing, 2φ , of the streamlines passing through the stagnation point, according to

$$\lambda_N = \tan^2 \varphi. \quad (11)$$

The present two-roller can, in general, be used [10] with a pair of rollers chosen from a set of eight such pairs of different diameters covering $0 \leq \lambda \leq 0.25$. For this study, the dimensions of the rollers used are specified in Table II, which corresponds to $\lambda = \lambda_N = 0.1501$ for a Newtonian fluid. The subscripts “th” and “exp” in Table II refer to the theoretical and experimental values, respectively. Eqns. (9) and (10) allow us to estimate the theoretical value of $(\dot{\gamma}_N/\omega)_{\text{th}}$ for this set of rollers, as given in Table II.

The stepping motor is interfaced to a computer (Hewlett Packard, model 9133 for TCFB or PC-486 for DLS) via a GPIB (National Instruments, U.S.A., model NI-488.2) switch board as shown in Fig. 5. The motor has a fast response time of $\mathcal{O}(10 \text{ ms})$ and a maximum acceleration of $100\,000 \text{ steps s}^{-2}$. Gears with reduction ratios 5 : 1 or 20 : 1 are used between the motor and the flow device to cover a wide range of velocity-gradients. The accuracy involved in repositioning of the flow cell with respect to the incident beam, even when it is dismounted for the purpose of replacing the solution, is always better than 0.0025 cm. in x , y and z directions (as defined by three translation stages used to control the respective movements) and 0.001 rad in the azimuthal orientation ϕ of the flow-cell (defined by the micrometer used to control the orientation) [Fig. 4]. The flow-cell was thermostated within $\pm 0.2^\circ\text{C}$ via a temperature-regulated waterbath circulator.

3. Dynamic light scattering

The optical setup for the dynamic light scattering experiment was built around the TCFB apparatus, as can be seen from Fig. 5, by mounting the necessary optical accessories on a triangular optical rail placed on the rotating arm of a massive goniometer that defines the scattering angle, θ , and hence the scattering vector \vec{q} [$q \equiv |\vec{q}| = \frac{4\pi n}{\lambda_B} \sin(\theta/2)$ as shown in Fig. 4, where n is the refractive-index of the solution]. The green beam of the laser is blocked using a beam stop near P_G , in Fig. 5. The incident blue beam scattered by the sample is polarized and collimated to project an image of the scattering volume at the photomultiplier tube (PMT) [Hamamatsu, model R647-04]. A blue line filter, F_B , obstructs any spurious light from reaching the detector. The preamplified and discriminated PMT pulses are fed to a 72-channel correlator (Brookhaven Instruments, U.S.A., model BI-2030) to construct time-resolved intensity autocorrelation functions. The commercial correlator software has been modified and used in PC-486 computer to control the flow experiment, as well as to analyze the correlation functions [7].

Provided that the seed particles are isotropic scatterers, and the time scale associated with the velocity-gradient [$t_\gamma \sim (q\dot{\gamma}L)^{-1}$, where L is the laser beamwidth]

is much smaller than the time scale for diffusive motion [$t_D \sim (Dq^2)^{-1}$], the homodyne intensity correlation function for a general linear flow in the beam coordinates (x', y', z') [Fig. 4] is given by [14,7]

$$F_2(\vec{q}, t) = \beta' \left| \int \int \int d^3\vec{r}' I(\vec{r}') \exp\{-i\vec{q}' \cdot \nabla \vec{v}' \cdot \vec{r}' t\} \right|^2. \quad (12)$$

Here, β' is the coherence factor defined by the optical geometry [28]. The velocity-gradient tensor $\nabla \vec{v}$ of Eqn. (6) can be expressed in the beam coordinates as

$$\nabla \vec{v}' = \mathbf{Q} \cdot \nabla \vec{v} \cdot \mathbf{Q}^T \text{ where } \mathbf{Q} = \begin{bmatrix} \cos \phi & -\sin \phi \\ \sin \phi & \cos \phi \end{bmatrix}. \quad (13)$$

In Fig. 4, the beam coordinates are chosen such that the scattering vector \vec{q}' is orthogonal to the y' axis, i.e.,

$$\vec{q}' \cdot \nabla \vec{v}' \cdot \vec{r}' = q_x f(\phi) x' + q_y g(\phi) y', \quad (14)$$

where $q_x = q \cos(\theta/2)$, $f(\phi) = \cos \phi (\epsilon \cos \phi - \dot{\gamma} \lambda \sin \phi) - \sin \phi (\dot{\gamma} \cos \phi + \epsilon \sin \phi)$ and $g(\phi) = \sin \phi (\epsilon \cos \phi - \dot{\gamma} \lambda \sin \phi) + \cos \phi (\dot{\gamma} \cos \phi + \epsilon \sin \phi)$.

Using a Gaussian intensity profile, Eqns. (13) and (14) in Eqn. (12), we get

$$F_2(\vec{q}, t) = \beta \exp \left\{ -\frac{1}{2} L^2 q^2 t^2 \cos^2 \left(\frac{\theta}{2} \right) h(\phi) \right\}, \quad (15)$$

where $\beta \propto \beta' L^6 \csc^2 \theta$ and

$$h(\phi) = f^2(\phi) + g^2(\phi). \quad (16)$$

The values of $h(\phi)$ are evaluated in Table III for three different azimuthal orientations of the two-roll mill. Thus, with the assumption of a symmetric flow [Eqn. 7], $\dot{\gamma}$ can be obtained from the decay rate $h(\phi)$ of the measured correlation function [Eqn. (15)] at one orientation, $\phi = 0$, of the flow-cell and λ from an additional measurement at a second orientation, $\phi = 90^\circ$ (see, Table III). The correlation functions were accumulated only after the flow had attained its steady value for the corresponding motor speed. To improve the signal to noise ratio, each correlation function was obtained by averaging over many repetitions of the experiment, ranging from a minimum of 200 repetitions at the high roller speeds, up to a maximum of 800 repetitions at the low roller speeds. Using a simulated annealing Monte Carlo fitting procedure [29], these average correlation functions were then fitted to Eqn. (15). In order to verify that the experimentally obtained correlation functions are very close to exponential in nature so that the above procedure followed to extract the velocity-gradient components from the decay time is indeed justified, we required a correlation coefficient R^2 , specifying the quality of the fit, exceeding 0.99.

Contrary to the basic assumption of optical isotropy of scatterers used to derive Eqn. (15), Wang et al [7] had

shown that this equation could also be used for the scattering from (intrinsically anisotropic) polymer molecules. In that case, the pre-exponential factor β is shown to be directly related to the components of the intrinsic molecular polarizability tensor.

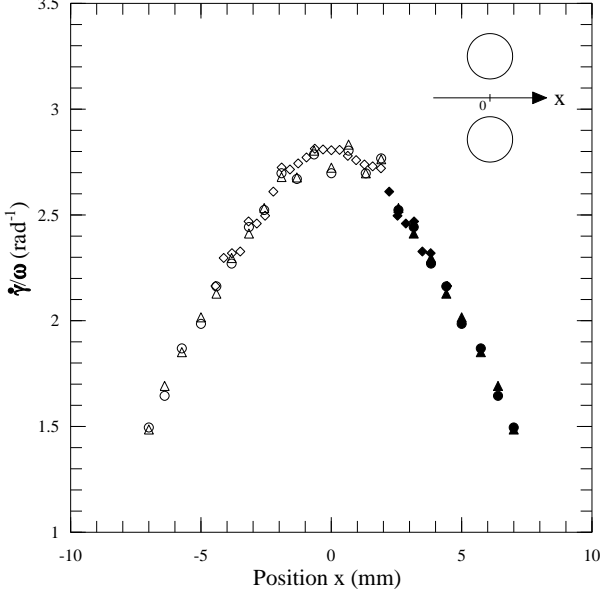


FIG. 6. The velocity-gradient profile along the central crossing line of the rollers with $\lambda = 0.1501$ and $\phi = 0^\circ$ for the Newtonian fluid at $\omega = 1.07$ rad/s (triangles and circles) and $\omega = 1.57$ rad/s (diamonds). The stagnation point was defined as the zero position. The hollow symbols denote the measured data and the filled symbols denote the data obtained by symmetry.

III. RESULTS

A. DLS steady flow results

1. Flow characterization

The DLS technique provides us the opportunity to map the flow-field in a large region between the rollers. In order to look for changes in the steady flow-field due to viscoelasticity in the presence of polymers compared to that seen with a Newtonian fluid, we first characterize the flow using a Newtonian fluid. This provides a comparison with predictions from the creeping flow theory for an unbounded two-roll mill. The measured velocity-gradient $\dot{\gamma}$ along the x axis through the stagnation point of the two-roll mill orientated at $\phi = 0^\circ$ for an angular velocity $\omega = 1.57$ rad/s is plotted along with two sets of data obtained by Wang et al [7], in terms of $\dot{\gamma}/\omega$ in Fig. 6. The filled symbols denote the points where the geometric construction of the flow-cell did not allow measurements, and those points are therefore obtained by the symmetric reflection of the hollow measured points at negative

x values. As can be clearly seen from this figure, different sets of experimental results obtained at widely separated times with different roller rotation rates overlap perfectly. In a small region surrounding the stagnation point the velocity-gradient were approximately constant, $\dot{\gamma}/\omega = 2.8$, certifying that the flow-field in this region is nearly homogeneous. Also, this value compares very well with the theoretically expected value of $\dot{\gamma}_N/\omega = 2.7$ (Table. II). From here onwards, we shall use $\dot{\gamma}_N$ and λ_N in the text to specify the values of $\dot{\gamma}$ and λ [Eqns. (9) and (10)] at the stagnation point of a two-roll mill filled with a Newtonian fluid, and the imposed motor speed will be measured in terms of the corresponding Newtonian strain-rate $\dot{\gamma}_N\sqrt{\lambda_N}$.

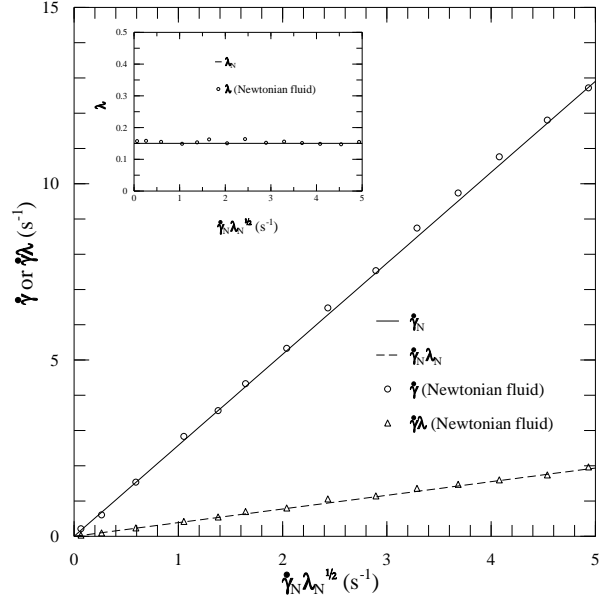


FIG. 7. Linear dependence of the magnitude of the velocity-gradient components, $\dot{\gamma}$ and $\dot{\gamma}\lambda$ (both in the units of s^{-1} and measured at $\phi = 0^\circ$ and $\phi = 90^\circ$, respectively), on the Newtonian rates of deformation, $\dot{\gamma}_N\lambda_N^{1/2}$ (in s), for a particular set of the rollers, $\lambda_N = 0.1501$, in steady flow at the stagnation region for the Newtonian fluid. The inset shows the strain-rate dependence of the flow-type parameter, λ , obtained by dividing one set of data by the other. The straight lines represent the creeping flow solutions.

In Fig. 7, we show the theoretical predictions for $\dot{\gamma}_N$ and $\dot{\gamma}_N\lambda_N$ [Eqn. (9), (10) and Table II] versus $\dot{\gamma}_N\sqrt{\lambda_N}$ in the form of straight lines. The experiments were carried out for 14 different Newtonian strain-rates, and for both parallel and perpendicular orientations of the sample cell. To extract the experimental values of $\dot{\gamma}$ and $\dot{\gamma}\lambda$ from the measured decay rates of the correlation function of Eqn. (15) at $\phi = 0^\circ$ and 90° respectively, we required a value for the beamwidth L . With an initial guess of $L = 29 \mu m$, that was reported for a previous set of experiments [7] from this laboratory, we used a simulated annealing Monte Carlo fitting technique [29] to

find via the fit shown in Fig. 7 that $L = 32 \mu\text{m}$ yields the best match of the theoretical straight lines for both $\dot{\gamma}$ and $\dot{\gamma}\lambda$ over the entire range of experimental strain-rates. Compared to the previous experiments [7], we have performed the present experiments including much higher motor speeds. It is clearly seen in the figure that the corresponding data agrees well with the creeping flow solution. The inset shows that the extracted value of the flow-type parameter λ also maintains a constant value as expected.

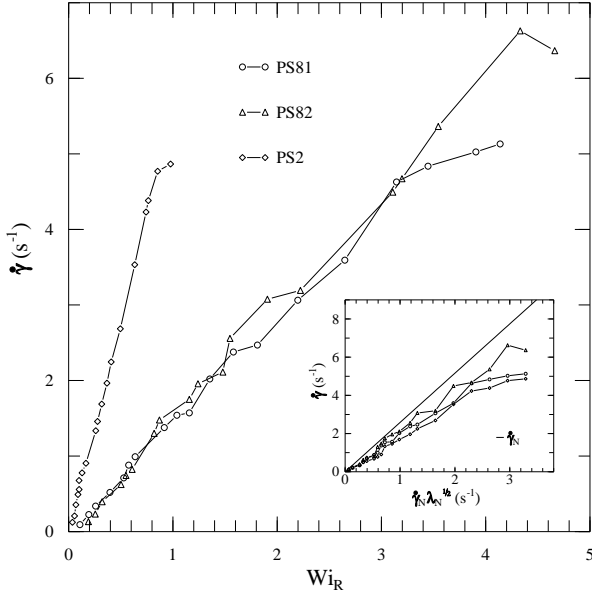


FIG. 8. The dependence of the velocity-gradient, $\dot{\gamma}$ (in s^{-1}), on the Weissenberg number $Wi_R = \dot{\gamma}\lambda^{1/2}\tau_R$ (based on the Rouse time, τ_R and the measured $\dot{\gamma}$ & λ), for $\lambda_N = 0.1501$, in steady flow at the stagnation region for the three entangled polystyrene fluids. In the inset, the same data are plotted versus the Newtonian rates of deformation, $\dot{\gamma}_N\lambda_N^{1/2}$ (in s^{-1}), and are compared with the creeping flow solution for $\dot{\gamma}_N$ (straight line).

In a similar manner, the flow parameters are measured for the three polymeric samples, PS81, PS82, and PS2, subjected to steady-state flow conditions. The results are plotted in Figs. 8, 9, and 10 versus the non-dimensionalized deformation rate, $Wi_R = \dot{\gamma}\sqrt{\lambda}\tau_R$, called the Weissenberg number (based on the Rouse time, τ_R , and *measured* values of $\dot{\gamma}$ and λ). The Weissenberg number is defined as the ratio of a characteristic relaxation time for the polymeric fluid to a characteristic time for deformation. It specifies the ability of a flow to generate departures of the polymer configuration from its static equilibrium value. The same data are also plotted against $\dot{\gamma}_N\sqrt{\lambda_N}$, in the inset of these figures, for a comparison with the Newtonian values shown by the straight lines. As expected, there is a substantial reduction in both $\dot{\gamma}$ and $\dot{\gamma}\lambda$ from the corresponding Newtonian value. The deviation from the Newtonian values increases with the

increasing roller rotation rate. Somewhat unexpectedly, however, both $\dot{\gamma}$ and $\dot{\gamma}\lambda$ still appear to increase approximately linearly with the Newtonian strain-rate. It is also noteworthy that this increase is very similar for the two samples, PS81 and PS2, which have the similar number of entanglements ($N_e \sim 13$) per chain (see, Table I). On the other hand, PS82, with $N_e \sim 7$ shows a different slope for its almost linear increment with increasing $\dot{\gamma}_N\sqrt{\lambda_N}$. When plotted against the Weissenberg number (Figs. 8 and 9), the qualitative feature of the curves for $\dot{\gamma}$ and $\dot{\gamma}\lambda$ appear to be quite different than that against $\dot{\gamma}_N\sqrt{\lambda_N}$: they become much more linear and owing to an order of magnitude smaller τ_R , the increment for PS2 with the increasing rate of deformation is much steeper than the other two samples. Also, $\dot{\gamma}$ versus Wi_R data for the two samples with similar molecular weight but different N_e are similar up to $Wi_R \sim 3$. The quantitative similarity in deformation rate dependence for the samples with similar N_e is more apparent for the flow-type parameter λ , as can be seen in Fig. 10. The qualitative nature of this dependence for all three samples appears to be similar, namely, it reaches an almost constant value (~ 0.1 for the samples with $N_e \sim 13$ and ~ 0.05 for PS82) at high deformation rates $Wi_R \geq 0.4$ ($\dot{\gamma}_N\sqrt{\lambda_N} \geq 1$) and at low rates of deformation exceeds the Newtonian values. There is an intermediate transition regime between these two different behaviors. The parameter λ attaining values higher than the Newtonian value at the lowest Wi_R studied, seems surprising since in the limit of extremely low deformation rate ($Wi_R \rightarrow 0$), one should expect even a Non-Newtonian fluid to exhibit Newtonian behavior. We are still away from this limit in that the Weissenberg number corresponding to the lowest motor speeds for the steady flow experiments are ~ 0.05 (PS2), ~ 0.1 (PS81) and ~ 0.2 (PS82). As mentioned earlier, each data point in $\dot{\gamma}$ and $\dot{\gamma}\lambda$ curves are obtained by averaging over several repeated experiments and then the λ values are obtained by point to point division of the two. Following a similar procedure, we have calculated the error-bars on the λ values from the standard deviations of the repeated experiments for $\dot{\gamma}$ and $\dot{\gamma}\lambda$ and plotted in Fig. 11. As expected, the error-bars increase for lower Wi_R , because of the division of smaller values of the corresponding $\dot{\gamma}\lambda$ by $\dot{\gamma}$. Even within the limits of these error-bars we can clearly see that λ initially exceeds λ_N . We have confirmed that this finding is not an experimental artifact by two other experimental means employed in this study, namely, the measurements of birefringence and flow parameters in transient flow conditions, and is described in section III.A.3 of this paper.

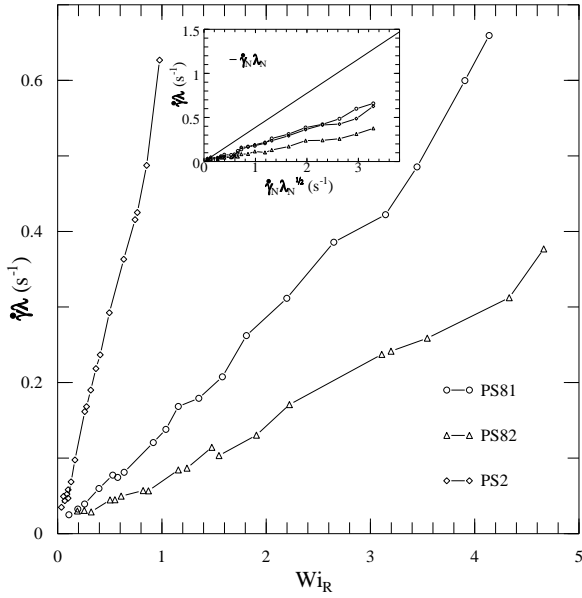


FIG. 9. The dependence of the component of velocity-gradient measured at $\phi = 90^\circ$, i.e., $\dot{\gamma}\lambda$ (in s^{-1}), on the Weissenberg number $Wi_R = \dot{\gamma}\lambda^{1/2}\tau_R$, for $\lambda_N = 0.1501$, in steady flow at the stagnation region for the three entangled polystyrene fluids. In the inset, the same data are plotted versus the Newtonian rates of deformation, $\dot{\gamma}_N\lambda_N^{1/2}$ (in s^{-1}), and are compared with the creeping flow solution for $\dot{\gamma}_N\lambda_N$ shown by the straight line).

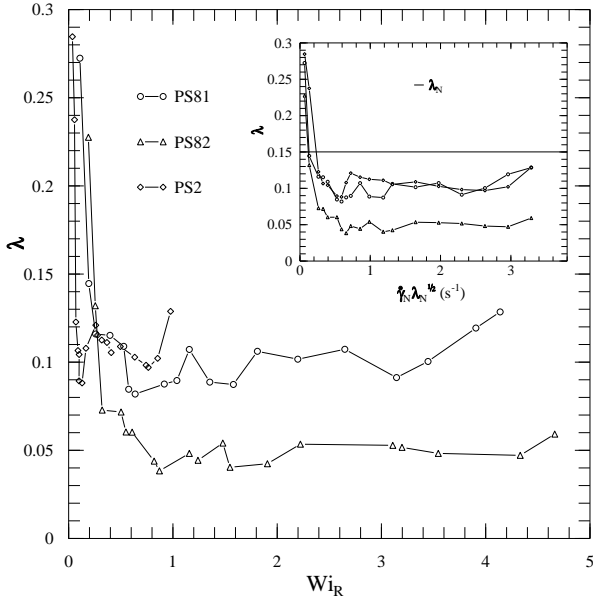


FIG. 10. The flow-type parameter λ versus Wi_R for $\lambda_N = 0.1501$, in steady flow for the three entangled polystyrene fluids, extracted by dividing the data in Fig. 8 by the corresponding data in Fig. 7. The inset shows the same data, plotted against $\dot{\gamma}_N\lambda_N^{1/2}$ (in s^{-1}) and compared with the creeping flow solution of $\lambda_N = 0.1501$ (straight line).

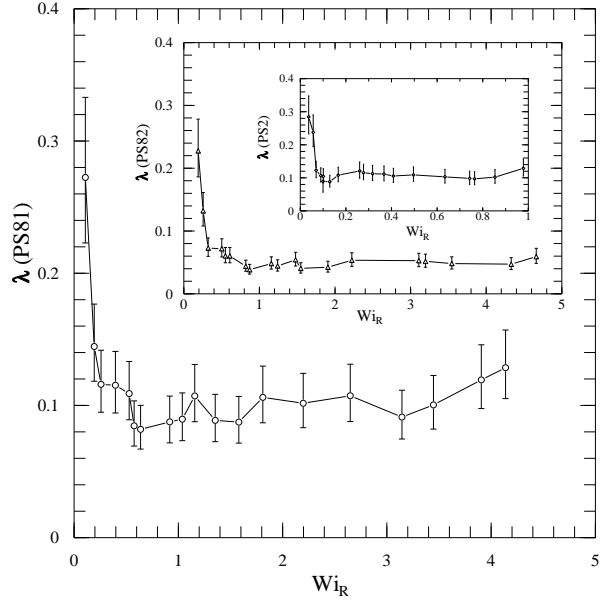


FIG. 11. The error-bars represent the standard deviation on the flow-type parameter, λ , measured at several Weissenberg numbers, Wi_R , for the steady-state flow of the entangled polymeric solutions.

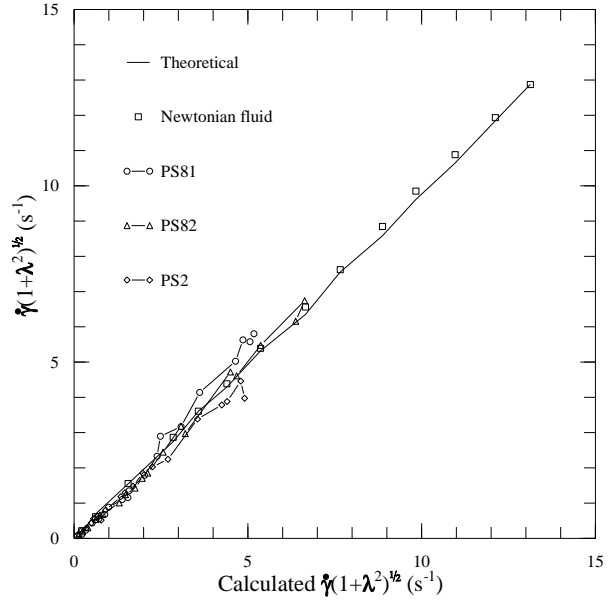


FIG. 12. The connected symbols illustrate the dependence of the velocity gradient component measured at $\phi = 45^\circ$, i.e., $\dot{\gamma}(1+\lambda^2)^{1/2}$, against its expected value, calculated using $\dot{\gamma}$ and λ values measured at $\phi = 0^\circ$ and $\phi = 90^\circ$, respectively, for the three entangled polystyrene fluids in steady flow at the stagnation region. In a similar fashion, the experimental and the theoretical (creeping flow) data for the Newtonian fluid are shown by the hollow squares and the solid line, respectively.

2. Flow symmetry

As we have mentioned before, the assumption that the flow in the two-roll mill is symmetric about the plane passing exactly midway between the co-rotating rollers (x, z) plane in Figs. 3 and 4) is valid for the creeping flow of a Newtonian fluid. For a viscoelastic fluid, one might expect the symmetry of the flow to change compared to the Newtonian case. Using the measured values of $\dot{\gamma}$ and $\dot{\gamma}\lambda$ (Figs. 8 & 9) at several different steady Newtonian strain-rates, we have calculated the expected values of $\dot{\gamma}\sqrt{(1+\lambda^2)}$. Then, by repeating exactly same steady flow conditions that were used to measure $\dot{\gamma}$ and λ , we have extracted the velocity-gradient component $\dot{\gamma}\sqrt{(1+\lambda^2)}$ from the decay rates of the correlations functions measured directly with the two-roll mill oriented at $\phi = 45^\circ$ (see, Table III). The result is plotted versus the corresponding calculated values at the same Newtonian strain-rates with the connected hollow symbols in Fig. 12 for the three viscoelastic samples. The hollow squares represent the measured values of $\dot{\gamma}\sqrt{(1+\lambda^2)}$ for the Newtonian fluid at $\phi = 45^\circ$. Both these and the theoretical values, i.e., $\dot{\gamma}_N\sqrt{(1+\lambda_N^2)}$ (shown by the solid line) at several strain-rates are plotted in Fig. 12 against the expected values of the same parameter that are calculated using the measured $\dot{\gamma}$ and $\dot{\gamma}\lambda$ data from Fig. 7. If the symmetry of the flow is maintained, then Eqn. (15) should be strictly valid for all orientations, ϕ , of the flow-cell. This means that each curve in Fig. 12 should be linear. As can be clearly seen from the figure, this is best followed for the Newtonian fluid indicating the fact that the flow is symmetric in this case, as expected. On the other hand, the data for the entangled fluids indicate that the flow symmetry is maintained only approximately, i.e., within the experimental accuracy of 10%, for the first five or six data points (i.e., for $\dot{\gamma}_N\sqrt{\lambda_N} < 0.5 \text{ s}^{-1}$). The data for PS81 and PS2 (both with $N_e \sim 13$) deviate more from the linearity with the increase of $\dot{\gamma}_N\sqrt{\lambda_N}$, but for PS82 ($N_e \sim 7$) the experimental data are fairly close to a straight line over the entire range of strain-rates studied. At high rates of deformation, the measured $\dot{\gamma}\sqrt{(1+\lambda^2)}$ is higher than the expected value for PS81 and PS82, but is lower in the case of PS2.

In order to quantify how flow symmetry changes with the deformation rate, we now proceed to evaluate the parameter ϵ of Eqn. (6). To do this, we can first extract the values for $h(\phi = 0^\circ)$, $h(\phi = 45^\circ)$ and $h(\phi = 90^\circ)$ from the experimentally measured decay rates of the correlation function at the three aforementioned orientations of the two-roll mill. When these values are used in conjunction with Table III, we get three equations involving the three unknowns $\dot{\gamma}$, λ and ϵ . We have used the Newton-Raphson's method [30] to numerically solve these equations for the case of a Newtonian fluid as well as for a representative case of the viscoelastic fluids of our study,

namely, for PS2. The results are shown in Fig. 13. Our experiments with a Newtonian fluid shows that ϵ is zero, i.e., the flow is perfectly symmetric, for strain-rates upto about 2 s^{-1} . Then, as the deformation rate is increased the value of ϵ increases almost linearly, though its value remains extremely small ($\sim 10^{-5}$) even at the highest strain-rates studied, justifying the fact that, for a Newtonian fluid the flow-symmetry is maintained. This also explains why the first seven data points ($\dot{\gamma}_N\sqrt{\lambda_N} < 2 \text{ s}^{-1}$) for the Newtonian fluid in Fig. 12 lies on the theoretical solid line and then slightly deviates from the line for the higher values of $\dot{\gamma}_N\sqrt{\lambda_N}$. For a non-Newtonian fluid, on the other hand, the flow-symmetry is maintained for only up to $\dot{\gamma}_N\sqrt{\lambda_N} < 0.5 \text{ s}^{-1}$. Our transient flow experiments with these polymer solutions are carried out in this range of deformation rates (which corresponds to $Wi_R < 1$) and will be reported in a subsequent paper [31].

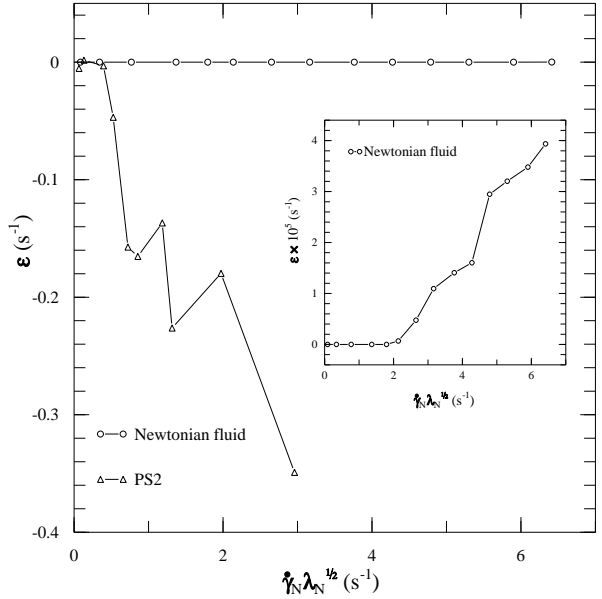


FIG. 13. The parameter ϵ versus the Newtonian strain-rate, $\dot{\gamma}_N\lambda_N^{1/2}$, for a representative polystyrene fluid PS2 and the Newtonian fluid. The inset shows the “zoomed up” result for the Newtonian fluid.

3. Steady flow and flow-type parameter

Let us now look into the effect of the polymer solutions on the steady-state values of the flow-type parameter λ at different angular velocities of the rollers. We have briefly referred to this point in Fig. 10. Since, we have also performed extensive DLS and TCFB experiments on these samples subjected to transient flows [31], namely, the startup flows from rest, for several constant Weissenberg numbers ($Wi_R < 1$), it would be worthwhile to check how the asymptotic values of λ extracted from each of those different experimental techniques vary with

Wi_R and also how they compare with the steady flow results of Fig. 10. From the transient DLS experiments, we can directly get the asymptotic values of λ but for the TCFB experiments, we should follow an indirect method to calculate λ . This can be done because for $Wi_R < 1$ the flow retains its symmetry, as we have shown before. The steady-state orientation of the principal optic axis at appreciable strain-rates is expected to approach the out-flow axis of the flow, or, in other words, $\chi \rightarrow \chi' \approx \varphi$ [see, Fig. 3]. Hence, λ may be calculated from the asymptotic orientation angle, χ' , of the flow birefringence data [31] for the startup flows, via a relation similar to Eqn. 11, i.e.,

$$\lambda \sim \tan^2 \chi'. \quad (17)$$

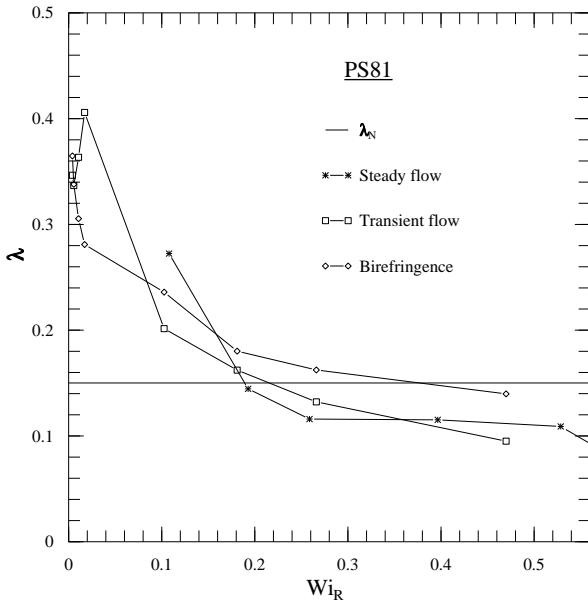


FIG. 14. The Weissenberg number ($Wi_R = \dot{\gamma}\lambda^{1/2}\tau_R$) dependence of the flow-type parameter, λ , for the polystyrene sample PS81, extracted from three different means (as explained in the text) and plotted together along with $\lambda_N = 0.1501$. The Weissenberg number is calculated based on the measured values of $\dot{\gamma}$, λ and τ_R .

We have presented the results in Figs. 14, 15 and 16 for the samples PS81, PS82, and PS2 respectively and compared the results with the theoretical value of $\lambda_N = 0.1501$. For each of these three polymeric samples, the overall qualitative match of the data as well as the quantitative match between the λ values calculated using three different experimental procedures, is quite satisfactory. The fair quantitative agreement between the asymptotic values of λ obtained from the transient flow experiments and the steady flow data for λ confirms that the startup experiments with the entangled samples have almost reached their steady values in the total predetermined evolution time of $t_e = 30$ s [31]. In agreement with the steady-state result, the transient experiments

also show λ values exceeding λ_N at the lowest rates of deformation studied, which again are higher than $Wi_R = 0$, where we should expect that $\lambda = \lambda_N$. In fact, for PS81, at the three lowest rates of deformations studied, the extracted value of λ from the transient experiments do show a trend to decrease after reaching a maximum.

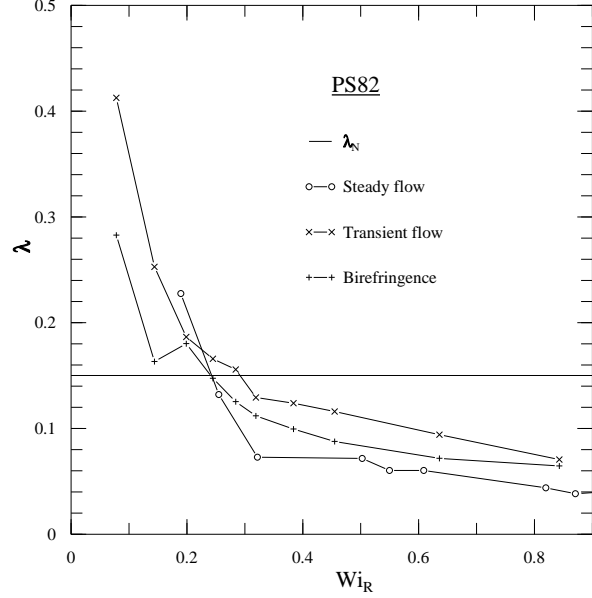


FIG. 15. Same as in Fig. 14, but for the polystyrene sample PS82.

B. The DEMG model comparison of the steady flow TCFB results

Probably one of the most used theoretical models to describe the dynamics of entangled polymers is the Doi-Edwards (DE) tube (reptation) model [17]. The primary drawback of this model, as is clearly evident by its failure to predict the polymer dynamics at high deformation rates $\dot{\gamma}\sqrt{\lambda} > 1/\tau_R$, is the fact that the primitive chain is assumed to be inextensible. Subsequently, in an effort to improve its predictions, the Doi-Edwards-Marrucci-Grizzuti (DEMG) model [27,23] was developed to incorporate chain-stretching into the original DE tube model. As noted earlier, the DEMG model contains two widely separated time scales, one for the relaxation of orientation (τ_d) and a much shorter one for the relaxation of the stretch of polymer segments (τ_R). Thus, as the strain-rate $\dot{\gamma}\sqrt{\lambda}$ is increased, segmental orientation takes place first when $\dot{\gamma}\sqrt{\lambda} \sim 1/\tau_d$ or $Wi_d = \dot{\gamma}\sqrt{\lambda}\tau_d = \mathcal{O}(1)$ and segmental stretching then “starts” at a much larger strain-rate when $Wi_R = \dot{\gamma}\sqrt{\lambda}\tau_R = \mathcal{O}(1)$. Also, it is expected that segmental orientation will take place earlier in dilute systems than in entangled systems. In agreement with the aforesaid expectations, a number of numerical studies [21] have suggested that the DEMG model has more success over the DE model when compared to ex-

perimental results for startup of a simple shear flow at high deformation rates ($Wi_R \geq 1$). Following this, in a recent numerical study [23,24], the DEMG model was developed further by “adding” a non-linear finitely extensible spring force.

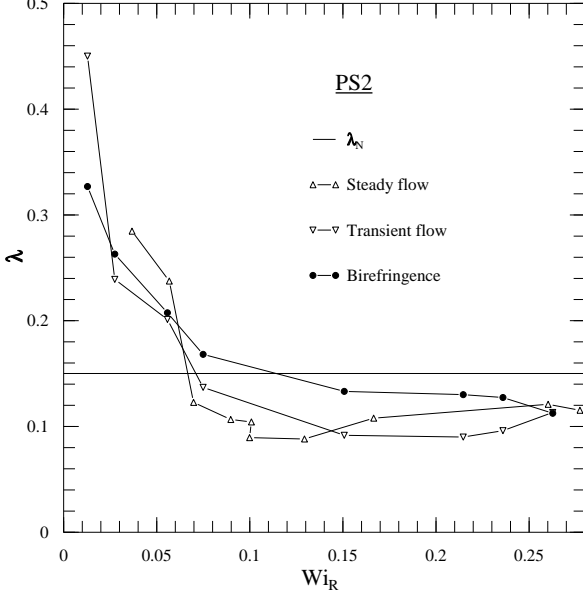


FIG. 16. Same as in Fig. 15, but for the polystyrene sample PS2.

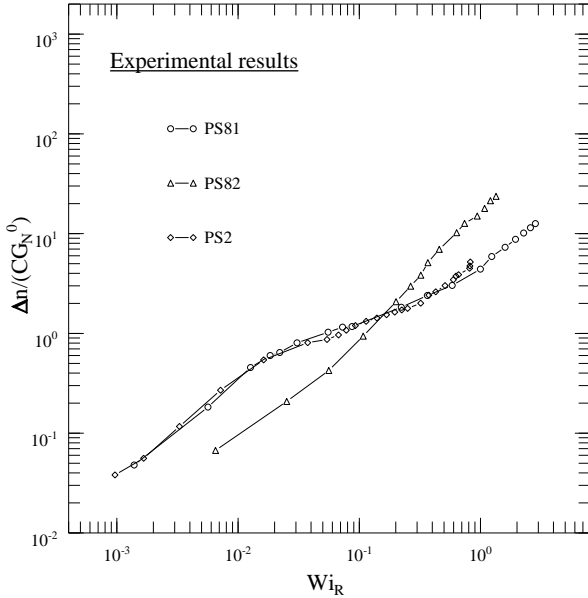


FIG. 17. The experimental steady-state birefringence data for the three entangled polystyrene solution plotted as functions of the Weissenberg number, $Wi_R = \dot{\gamma}\lambda^{1/2}\tau_R$, based on the measured magnitude of the principal eigenvalue, $\dot{\gamma}\lambda^{1/2}$, of the velocity-gradient tensor, $\nabla\vec{v}$, and the Rouse time scale, τ_R . The birefringence is normalized with CG_N^0 , where G_N^0 is the plateau modulus, and C is the stress-optical coefficient. The data are plotted in the same scale as the corresponding DEMG model predictions in Fig. 18.

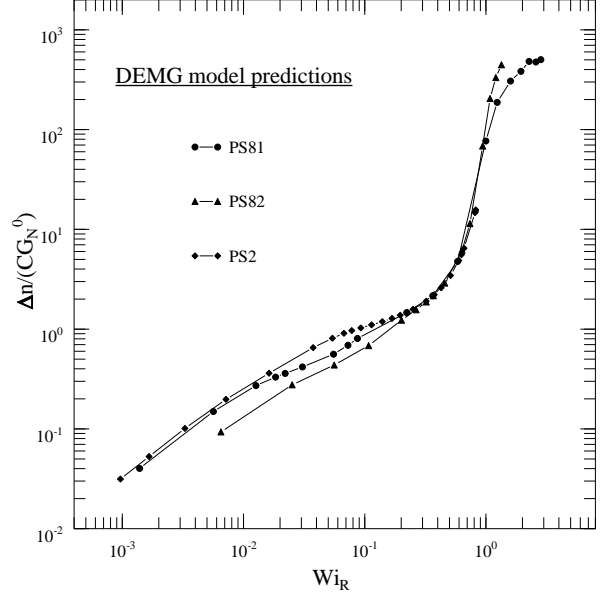


FIG. 18. The DEMG model predictions for the steady-state $\Delta n/(CG_N^0)$, using measured values of both $\dot{\gamma}$ and λ , at several different strain-rates Wi_R but the same set of rollers, $\lambda_N = 0.1501$, for the polystyrene samples. The model parameters n_t , N_e , and τ_R are given in Table I.

For an entangled solution, birefringence measurements directly relate to changes in the conformation of the polymer molecules. As mentioned earlier, the complete characterization of the flow-induced anisotropy of a polymeric fluid requires determination of the birefringence, Δn , as well as the orientation angle, χ , of the principal axes of the refractive index tensor. In this section, we present the steady-state two-color flow birefringence results and compare them with the predictions of the DEMG model using the flow parameters measured via DLS as input. We assume that the velocity-gradient tensor in $\sim 75\mu\text{m}$ diameter birefringence measurement zone surrounding the stagnation point of the co-rotating two-roll mill can be approximated by Eqn. (6) and (7). The values of the model parameters N_e , τ_R , and n_t calculated for the three solutions are given in the Table I. Here n_t is the number of Kuhn statistical subunits in the chain based on the assumption of 10 monomers per subunit and is calculated from the molecular weight of the polymer [32]. The steady-state experimental results for the dimensionless birefringence, $\Delta n/(CG_N^0)$, for the three entangled samples are presented in Fig. 17 as functions of Wi_R . The birefringence, Δn , is scaled by the birefringence CG_N^0 (obtained by using the stress-optical law) that would be present at a stress level equal to the plateau modulus, G_N^0 . Here, C is the stress-optical coefficient which in the free-jointed chain model is defined as

$$C = \frac{2\pi}{45} \left[\frac{(\bar{n} + 2)^2}{\bar{n}} \right] \langle \alpha_{\parallel} - \alpha_{\perp} \rangle, \quad (18)$$

where α_{\parallel} and α_{\perp} are the components of the intrinsic

molecular polarizability tensor $\underline{\alpha}(t)$ along and perpendicular to the Kuhn statistical segment, and \bar{n} is the bulk refractive-index of the medium. This is justified only up to a modest level ($\leq 50\%$) of fractional chain-extension, so that non-Gaussian effects can be neglected. To scale the experimental birefringence, an approximate expression given in Eqn. (2) for the plateau modulus, G_N^0 , and the literature value [8] of $C = 5 \times 10^{-10} \text{ cm}^2/\text{dyn}$ for polystyrene solutions is used. The model predictions corresponding to the experimental curves in Fig. 17 are displayed in Fig. 18 (both on the same scale). Each individual point on the predicted curves of Fig. 18 is the steady-state value obtained from separate runs of DEMG model numerical simulations using the measured values of $\dot{\gamma}$ and λ for each corresponding point on the experimental curves (Fig. 17). The model clearly predicts [24] the existence of three flow regimes in the steady-state, namely, the *linear viscoelastic* regime seen at low rates of deformation $Wi_d < \mathcal{O}(1)$, the *non-linear viscoelastic* regime seen at the intermediate deformation rates lying between $Wi_d > \mathcal{O}(1)$ and $Wi_R < \mathcal{O}(1)$, and the *highly non-linear viscoelastic* regime seen at high deformation rates $Wi_R > \mathcal{O}(1)$. In each of these flow regimes, the effect of three parameters, namely, n_t , N_e , and λ on the nature of deformation rate dependence of the birefringence, orientation angle, stretch and viscosity, as predicted by the DEMG model, has been discussed in detail in a recent publication by Mead *et al.* [24].

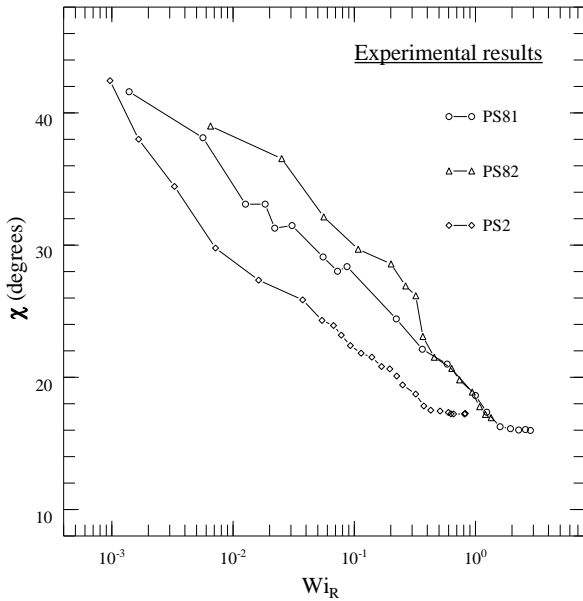


FIG. 19. The experimental steady-state orientation angle, χ (in degrees), for the three entangled polystyrene solution plotted as a function of the Weissenberg number, $Wi_R = \dot{\gamma}\lambda^{1/2}\tau_R$, using the measured values of $\dot{\gamma}$, λ and τ_R . The data are plotted in the same scale as the corresponding DEMG model predictions in Fig. 20.

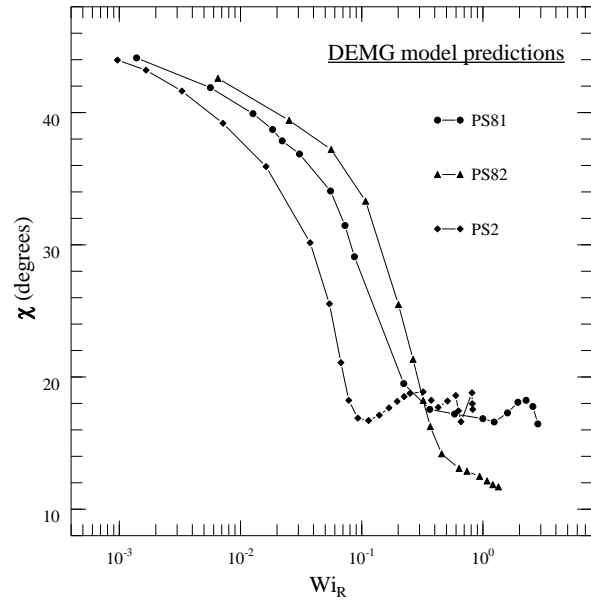


FIG. 20. The DEMG model predictions for the steady-state orientation angle, χ (in degrees), using measured values of both $\dot{\gamma}$ and λ , at several different strain-rates, Wi_R , for the three polystyrene fluids in a two-roll mill with a fixed set of rollers, $\lambda_N = 0.1501$. The model parameters n_t , N_e , and τ_R are given in Table I.

In the linear viscoelastic regime, the slope of each experimental curve on the double-logarithmic plots (Fig. 17) is indeed unity [24], similar to the predicted curves (Fig. 18). According to the predictions of Ref. [24], in this flow regime, the relative positions of the birefringence curves from top to bottom for these entangled samples is primarily determined by the values of N_e and λ (curves with lower N_e and higher λ will fall lower), while n_t has no effect. As clearly seen from Figs. 17 and 18, the lower value of N_e for PS82 keeps the $\Delta n/(CG_N^0)$ curve lower than those of the other two samples. The lower value of λ for PS82 in this regime (Fig. 10) would predict otherwise [24]. The slight difference between the curves for PS2 and PS81 (both having $N_e \sim 13$) seen both in the experimental and predicted plots, is due to the slight difference in the λ values between the two samples in this regime, as can be clearly seen from Fig. 10. In this flow regime, although the initial low levels of segmental orientation, as predicted in Fig. 20, is indeed seen for the experimental curves in Fig. 19, the rate of decrease of χ with increasing Wi_R , as seen in the experiments for all samples, is much faster than predicted. Also, the orientation angles for PS81 at a fixed value of Wi_R in this regime lies in between those for the other two liquids which again is in accord with the theoretical expectations [24] (taking into account the effects of the corresponding values of n_t , N_e and measured λ).

When the second flow regime of non-linear viscoelasticity is approached, $Wi_d = \mathcal{O}(1)$, the scaled birefringence curves are predicted to depart from linearity and begin

to approach a plateau, as seen in the DEMG results of Fig. 18. The width of the plateau is directly proportional to N_e , and is therefore expected to be about half as wide for PS82 ($N_e \sim 7$) as for PS2 and PS81 ($N_e \sim 13$). The experimental curves in this regime do show non-linearity for all three samples, but the collapse of the curves and an existence of a narrow plateau is seen only for PS81 and PS2 and not for PS82. The dynamics in this regime are controlled by strong segmental orientation of the tube without stretching. Referring to Fig. 19, we see that the monotonic decrease of the orientation angle with increasing Wi_R , seen in experiments for all samples is in qualitative agreement with the predictions of the DEMG model, resulting from the gradual unwinding and straightening out of the tube. The relative positions of the χ versus Wi_R curves from top to bottom in Fig. 20 for the three samples are the result of a competition between the effects of N_e and λ them. Having a lower value of λ (see, Fig. 10) prompts [24] the orientational angle for PS82 to fall below those for the other two samples, but as can be seen in Figs. 19 and 20, the effect of N_e is stronger in this case too, since the curves with a lower value of N_e (that for PS82, here) are predicted [24] to show a lower degree of orientation at any fixed Wi_R in this flow regime. Similarly, PS2 exhibits a higher degree of orientation than for PS81 at a fixed Wi_R , since λ is lower for PS2 in this intermediate regime of flow. As $Wi_R \rightarrow 1$, the tube is expected to straighten out to its full length and become orientated in the direction of the outflow axis [Fig. 3] with the orientation angle reaching its asymptotic value, χ' , given in Eqn. (17). Using the asymptotic values of $\lambda \sim 0.1$ for PS2 and PS81 and $\lambda \sim 0.05$ for PS82 from Fig. 10, we obtain $\chi' \sim 17.55^\circ$ for PS2 and PS81 and $\chi' \sim 12.60^\circ$ for PS82 which are in agreement with the results in Fig. 20. Interestingly, the theoretical predictions for the orientation angles for PS2 and PS81 in Fig. 20 show an “undershoot” before reaching χ' . For the highest rates of deformation, $Wi_R \sim 1.5$, studied for PS82, the predicted orientation angle has not reached its asymptotic value. The experimental curves of χ , as seen in Fig. 19, qualitatively follow the behavior shown by the predicted curves except for that they do not show an undershoot behavior. In addition, $\chi' \sim 17.5^\circ$ and $\chi' \sim 16^\circ$ for PS2 and PS81, respectively and although the final value of χ at the highest Wi_R studied for PS82 is $\sim 17.4^\circ$, it does not seem to have saturated; and for $0.3 < Wi_R \leq 1.5$ the χ values for PS81 and PS82 overlap.

The third flow region of highly non-linear viscoelasticity ($Wi_R \geq 1$) is predicted [24] to show three distinct signatures. Firstly, the tube orientation should be complete as indicated by $\chi = \chi'$. We have discussed about the behavior of the predicted and experimental orientation angles for all polystyrene samples in the preceding paragraph. Secondly, the onset of chain-stretching is predicted to take place with a clear evidence of the dimensionless birefringence exceeding its plateau value of

unity as shown in Fig. 18. This is evident in the experiments too, as displayed in Fig. 17. Thirdly, the onset of chain-stretching is also marked by the collapse of all the birefringence curves to a single universal curve at the end of the plateau i.e., they should follow the scaling behavior $\Delta n / (CG_N^0) = f(Wi_R)$ in this region, as is clearly shown by the predicted traces in Fig. 18. This feature is well demonstrated in the experiments (Fig. 17) by PS81 and PS2 but not by PS82, which fails to show a well-defined plateau too. At high rates of deformation ($Wi_R > 1$), the chain-stretching dynamics prompts the different birefringence curves to reach different asymptotes proportional to $\sim n_t / N_e$. The theoretical curves in Fig. 18 show these features: the increase in the birefringence with Wi_R in this regime is faster for PS82 ($n_t = 8420$ and $N_e \sim 7$) than for PS81 ($n_t = 8420$ and $N_e \sim 13$), which is in turn faster than for PS2 ($n_t = 2890$ and $N_e \sim 13$). However, none of the $\Delta n / (CG_N^0)$ curves are predicted to reach their asymptotic values (~ 648 for PS81, ~ 1203 for PS82 and ~ 222 for PS2) for the highest Wi_R studied, though the curves for PS81 and PS82 indeed show a tendency towards saturation in Fig. 18. At the highest rates of deformations, the experimental birefringence levels (Fig. 17) for all samples are significantly below their saturation values, and they do not show a tendency to saturate. Contrary to the prediction, the experimental $\Delta n / (CG_N^0)$ curve for PS81 falls below that for PS2. We note that the relative level of birefringence for the different samples as depicted by the individual curves in Figs. 17 and 18 are strongly dependent on the choice of the value of the relaxation modulus, G_N^0 [Eqn. (2)]. However, we believe that the qualitative as well as quantitative agreement between the experimental and predicted birefringence curves well justifies the choice of value for G_N^0 .

Following Mead et al. [23], we define the generalized viscosity function (which is the conventional viscosity appropriately generalized for mixed shear and extensional flow) as follows:

$$\eta(\dot{\gamma}, \lambda) = \frac{\sigma_{xy}}{\dot{\gamma}(1 + \lambda)}. \quad (19)$$

This reduces to the usual definition of the shear viscosity and the planar extensional viscosity in the limits of $\lambda = 0$ and $\lambda = 1$, respectively. The scaling factor $(1 + \lambda)$ makes the viscosity independent of the flow-type λ at low strain-rates. In the principal axes of the rate of deformation tensor, which are at 45° from the coordinate axes used in Figs. 3 and 4, we get $\eta(\dot{\gamma}, \lambda) = \frac{\sigma'_{xx} - \sigma'_{yy}}{\dot{\gamma}(1 + \lambda)}$. Using the stress-optical relationship [8], which states that the birefringence tensor is proportional and coaxial to the stress tensor, one can relate the birefringence, which is the difference of the principal values of the refractive-index tensor, \underline{n} , in the plane of the flow (i.e., $\Delta n = n'_{xx} - n'_{yy}$), to the stress as $\sigma_{xy} = \frac{\Delta n}{2C} \sin(2\chi)$, so that Eqn. (19) can be written as

$$\eta(\dot{\gamma}, \lambda) = \frac{\Delta n \sin(2\chi)}{2C\dot{\gamma}(1 + \lambda)}. \quad (20)$$

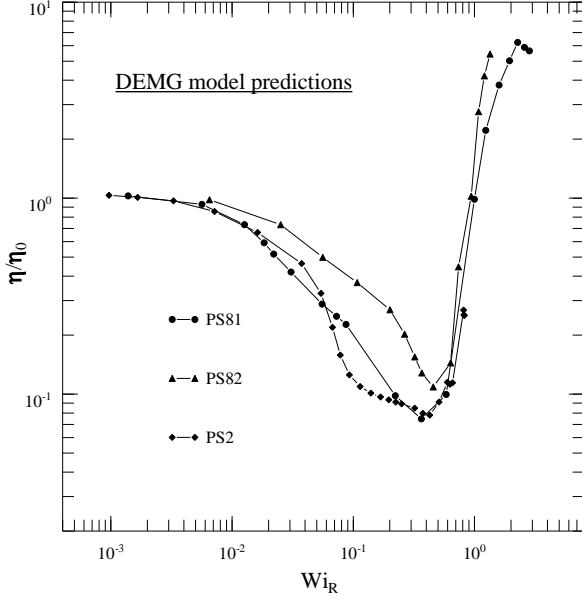


FIG. 21. The predicted behavior of the steady-state generalized extensional viscosity scaled with the zero-shear viscosity, as a function of Wi_R for the polystyrene solutions, obtained by using the computed values of Δn and χ from the DEMG model, the measured values of $\dot{\gamma}$ and λ , the stress-optical relationship, and the definitions of η and η_0 . The model parameters n_t , N_e , and τ_R are given in Table I.

We present the predicted and the experimental steady-state viscosity function versus the measured Wi_R for the three polystyrene solutions in Figs. 21 and 22, respectively. The predicted values of η are calculated from Eqn. (20) by using the predicted birefringence and extinction angle shown in Figs. 18 and 20, and by scaling the viscosity with the zero shear viscosity,

$$\eta_0 = \frac{G_N^0 \tau_d \pi^2}{45}. \quad (21)$$

Similarly the experimental plots shown in Fig. 22 are calculated with the use of the measured Δn (Fig. 17) and χ (Fig. 19) and then by normalizing by the experimental η_0 given in Table I. In sharp contrast to the observation [33] that dilute solutions, (e.g., Boger fluids) show strain-rate thickening at high strain-rates, for entangled solutions the viscosity function is predicted to show different behaviors in the three earlier defined flow regimes. In the first flow regime of linear viscoelasticity, the viscosity is predicted to be nearly constant and equal to its zero shear-rate value, η_0 , (Fig. 21). This is approximately followed by the experimental curves (Fig. 22). In the intermediate flow regime [between $Wi_d > \mathcal{O}(1)$ and $Wi_R < \mathcal{O}(1)$], where the stress is generated primarily via orientation of the tube segments, the model predicts a strong strain-rate thinning behavior with the degree of

thinning being an increasing function of N_e and a decreasing function of λ , as shown in Fig. 21. In the experiments, we see that N_e has a stronger effect than λ on the degree of thinning. The predicted effect of λ on the relative positions of η/η_0 versus Wi_R curves for PS81 and PS2 from top to bottom is not supported in the experiments.

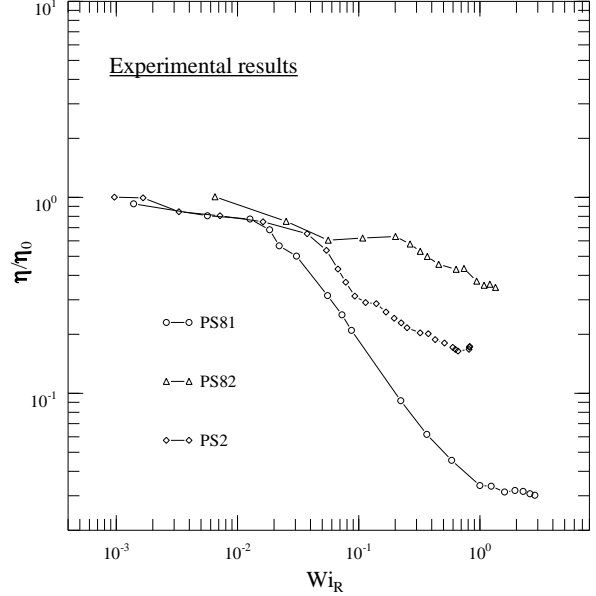


FIG. 22. The steady-state generalized extensional viscosity scaled with the zero-shear viscosity, versus Wi_R for the polystyrene solutions, obtained by using the experimentally measured values of Δn , χ , $\dot{\gamma}$, λ , η_0 , the stress-optical relationship, and the definition of η . The data are plotted in the same scale as the corresponding DEMG model predictions in Fig. 21.

The presence of an “undershoot” in the predicted orientation angle for PS2 (Fig. 20) in this flow regime clearly manifests itself in the predicted viscosity plot (Fig. 21) too. This does not seem to be the case with PS82, because for PS82 the small undershoot present in the predicted orientation angle does not show up in the predicted viscosity. Although, the experimental viscosity function shows a thinning behavior with the degree of thinning being much weaker in PS82 than the other two solutions, the model predicts much stronger viscosity thinning behavior than observed in the experiments (except for PS81 where they are similar). Also, the expected “undershoot” in the viscosity for PS2 is absent in the experiment.

In the third regime of flow [$Wi_R = \mathcal{O}(1)$] the model predicts a sharp upturn in the viscosity function as chain-stretching is predicted to take place. As the rate of deformation is increased, the viscosity is also expected to increase and finally reach an asymptote for $Wi_R \gg 1$. Surprisingly, however, except for a small upturn shown by the last three data points for PS2 in Fig. 22, these pre-

dicted features are completely absent in the experimental data. The cause for this lies in the fact that even though the experimental birefringence values of these samples (Fig. 17) rise above the plateau value, indicating chain-stretching, the rise is much weaker than predicted (Fig. 18). Also, the degree of orientation of the tube segments in the experiments (Fig. 19) fails to show the sharpness predicted by the model (Fig. 20) in this flow regime.

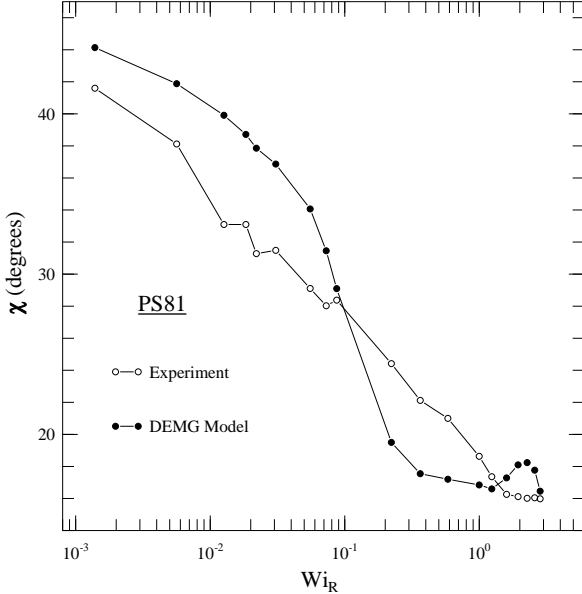


FIG. 23. A comparison of the Weissenberg number dependence of the measured steady-state orientational angle, χ (in degrees), with values predicted via the DEMG model using the measured values of both $\dot{\gamma}$ and λ for the PS81 solution. The model parameters were $N_e = 13$, $n_t = 8420$, and $\tau_R = 2.25$ s.

The above two effects compete with each other to nullify any signature of chain-stretching that could have been otherwise seen in the generalized viscosity function. We have noted before that the present model [23,24] has improved the original DEMG model by using finitely extensible freely jointed chains instead of infinitely extensible Gaussian chains. In the limit of the high value of n_t (or M_w), the original version of the model is retrieved and at high deformation rates the chains stretch tremendously to show a nearly singular viscosity or birefringence. This effect is apparent in the model predictions shown in Figs. 21 and 18, where both PS81 and PS82 (higher n_t or M_w) show a steeper increase in η and $\Delta n/(CG_N^0)$ at $Wi_R \sim 1$ compared to PS2, but is absent in the experiments (Figs. 22 and 17). Unfortunately, the highest dimensionless rate of deformation or Wi_R that we could reach in the experiments is only about 3 for PS81 and about 1 for the other two solutions. This deficiency is caused by the fact that the viscoelastic modification relative to the Newtonian flow was much stronger than we had initially expected. The measured values of

$\dot{\gamma}$ and λ were thus reduced compared to their Newtonian values, so that the originally calculated theoretical $(Wi_R)_N^{\max} \equiv (\dot{\gamma}_N \sqrt{\lambda_N \tau_R})^{\max} = \mathcal{O}(10)$ corresponding to the maximum motor speed chosen for the experiments ultimately produced only $(Wi_R)^{\max} \equiv (\dot{\gamma} \sqrt{\lambda \tau_R})^{\max} = \mathcal{O}(1)$. The absence of chain-stretching signatures in the viscosity may also have to do with the choice of sample compositions which gives rise to low values for the number of entanglements per chain. It would be interesting to carry out further experiments on samples with higher N_e in this highly non-linear viscoelastic flow regime at high enough Wi_R , particularly to look into the chain-stretching effects much more carefully.

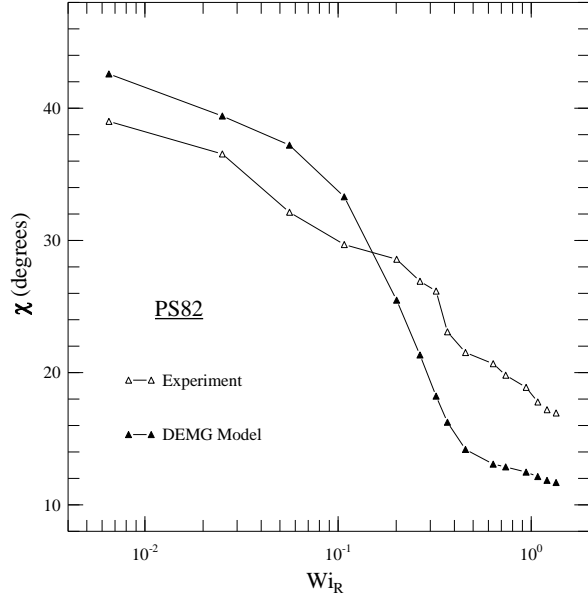


FIG. 24. The experimental data for the steady-state, χ (in degrees), versus Wi_R for the sample PS82 compared with the corresponding DEMG predictions, obtained by using the measured values of both $\dot{\gamma}$ and λ , and the model parameters $N_e = 7$, $n_t = 8420$, and $\tau_R = 3.01$ s.

Let us now turn our attention into more quantitative comparisons between the steady-state results and the predictions of the DEMG model. We will first consider the case of the orientation angle χ for three samples as shown in Figs. 23, 24, and 25. Since there is no other parameter involved for scaling (e.g., in the case of the birefringence), direct comparisons between the experimental data and model predictions are possible in this case. Although the experimental data follows a similar qualitative decreasing trend in the orientation angle with increasing Wi_R , as predicted, the quantitative mismatch with the prediction is quite obvious in these figures. In the limit $Wi_R \rightarrow 0$, it is expected that χ should be 45° , corresponding to alignment of the principal optical axis with the principal axis of the rate of strain tensor. The experimental accuracy of both Δn and χ at the lowest rates of deformation is limited by the sensitivity of the

apparatus in determining a minimum birefringence and its associated orientation. Also, the contribution from the residual glass birefringence is important at these low levels of polymer anisotropy. At low and intermediate Wi_R the DEMG model underpredicts the orientation but at higher Wi_R it overpredicts the same, and there is a crossing point between these two behaviors. By comparing the results on the orientation angle with those obtained from the DEMG model numerical simulations with identical parameters but with a constant flow-type parameter $\lambda = \lambda_N = 0.1501$, we have confirmed that the opposite curvatures seen in the predicted curves below and above the crossing point depends on the way λ changes with Wi_R . The fact that the DEMG model overpredicts the tendency of the flow to orient polymer chains towards the outflow axis at intermediate and high strain-rates has been observed in earlier experiments [12,13] and it was speculated that “tube-dilation”, which is not incorporated in the DEMG model, may be responsible for such an effect. In simple terms, this means that the effective dilation of the tube radius is stronger for large rates of deformation, leading to a reduction of N_e and hence the lower orientation angle seen in the experiments. Whether or not tube-dilation is present in the system, for $Wi_R \geq \mathcal{O}(1)$, we expect that the polymer molecules will become oriented along the outflow axis of the flow-field. As we have noted earlier, and as can be seen clearly from these figures, the asymptotic value of χ is approximately reached in experiments for PS81 and PS2, but not for PS82.

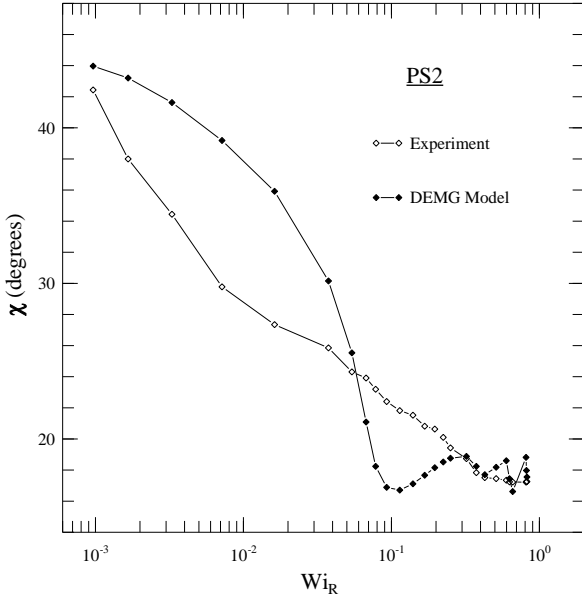


FIG. 25. A comparison of the Weissenberg number dependence of the measured steady-state orientational angle, χ (in degrees), with values predicted via the DEMG model using the measured values of both $\dot{\gamma}$ and λ for the PS2 solution. The model parameters were $N_e = 13$, $n_t = 2890$, and $\tau_R = 0.56$ s.

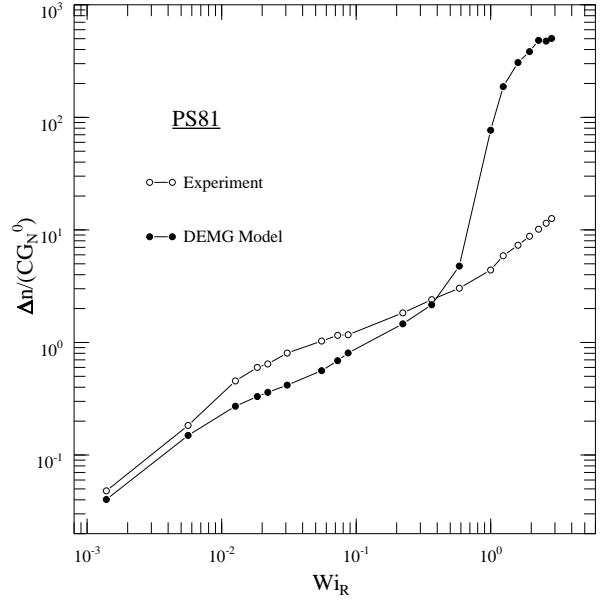


FIG. 26. A comparison of the measured steady-state scaled birefringence, $\Delta n/(CG_N^0)$ at several different Wi_R , with the values predicted via the DEMG model obtained by using the measured $\dot{\gamma}$ and λ for the PS81 solution. The model parameters used were $N_e = 13$, $n_t = 8420$, and $\tau_R = 2.25$ s.

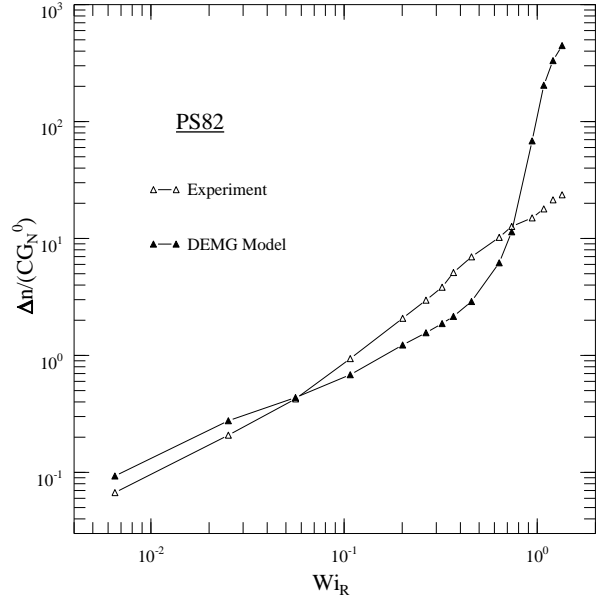


FIG. 27. The experimental data for the steady-state $\Delta n/(CG_N^0)$ versus Wi_R for the sample PS82 compared with the corresponding DEMG predictions, obtained by using the measured values of both $\dot{\gamma}$ and λ , and the model parameters $N_e = 7$, $n_t = 8420$, and $\tau_R = 3.01$ s.

The qualitative as well as quantitative match between the experimental and predicted birefringence curves for these entangled samples, shown in Figs. 26, 27 and 28, is quite satisfactory. This firstly points to the fact that the choice of the plateau modulus, as described earlier in this section, works very well for these entangled sys-

tems. Given the proper values of G_N^0 , we can clearly see that DEMG model predictions for birefringence are fairly close to the experimental measurements, at least for low and intermediate Wi_R . We note that the plateau expected in the transition region between the dynamics dominated by segmental orientation and segmental stretch, is quite narrow, because of the small separation between τ_d and τ_R ($\tau_d/\tau_R = 3N_e = 21$ for PS82, and 39 for PS81 & PS2). The plateau is smeared out in the experimental curves, since tube-dilation reduces N_e and hence the separation $3N_e$ between these two time scales. This supports the tube-dilation idea. In the nonlinear viscoelastic regime, the chain-stretching predicted by the model is much stronger than what has been seen experimentally. In the limit $Wi_R \rightarrow \infty$, the model predicts a saturation of birefringence $\sim n_t/N_e$ corresponding to a maximum chain-extension ratio $\sim \sqrt{n_t/N_e}$. Comparing the maximum birefringence shown in Figs. 26, 27, and 28 with the above numbers, we see that the maximum chain-extension predicted by DEMG model at the highest Wi_R studied are 87.8%, 63.2% and 28.5% for PS81, PS82 and PS2, respectively but the experimentally observed maximum chain-extension for these samples is only $\sim 15\%$.

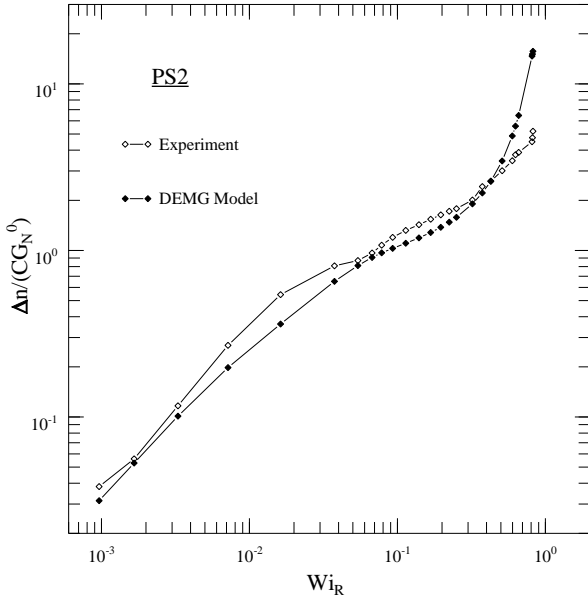


FIG. 28. A comparison of the Weissenberg number dependence of the measured steady-state birefringence, $\Delta n/(CG_N^0)$, with the corresponding DEMG model predictions obtained by using the measured values of both $\dot{\gamma}$ and λ for the PS2 solution. The model parameters were $N_e = 13$, $n_t = 2890$, and $\tau_R = 0.56$ s.

The quantitative agreement between the experimental and the predicted η/η_0 for small rates of deformation in Figs. 29, 30, and 31 directly points to a proper choice of the calculated and the experimental values of η_0 . In the intermediate flow regime the DEMG model predicts a strong strain-rate thinning behavior for the

generalized extensional viscosity for entangled solutions. This also distinguishes the entangled solution from dilute ones, for which a monotonic increase in η with the increase of $\dot{\gamma}$ is expected. In the experiments, we see that the solutions with $N_e \sim 13$ show much stronger thinning than the solutions with a lower value of N_e , consistent with the prediction. It has been shown in earlier experiments that the original DE model overpredicts the strength of shear-thinning in simple shear flows [13] and the DEMG model also shows a similar behavior in extension-dominated flows [12]. Similarly, we note that the excessive shear-thinning predicted by DEMG model for PS82 and PS2 (shown in Figs. 30 and 31, respectively) is due to the fact that the predicted orientation angle and the birefringence are too small in this intermediate range of Wi_R (see, Figs. 24, 25, 27 and 28). The tendency of DEMG model to over-orient the polymer chain away from the principle axis of the rate of strain tensor, is speculated [12,13] to be due to the fact that the model does not incorporate the tube-dilation effect which may be present in the real systems. For PS81, as can be seen from Fig. 29, the experimental curve for the viscosity closely follows the predictions of the DEMG model in the low and intermediate range of Wi_R primarily due to the fact that, in this region, Δn is too small but χ is too large so as to compensate each other. It can be seen from these figures that as Wi_R approaches $\mathcal{O}(1)$, the model predicts an upturn of the viscosity followed by a sharp increase owing to the prediction of a strong chain-stretching phenomenon. Apart from a small upturn seen in Fig. 31, the model fails to account for the observed behavior of the generalized extensional viscosity in this non-linear viscoelastic regime.

1. Cox-Merz superposition

The empirical Cox-Merz relation states that the steady shear viscosity is equal to the modulus of the complex dynamic viscosity evaluated at the angular frequency equal to the shear-rate. This is observed to be valid mostly in the linear viscoelastic regime [34], and also in the case of a simple shear flow ($\lambda = 0$), primarily because chain-stretching is not significant in either of these cases. Thus, for extensional flows ($\lambda > 0$) departure from Cox-Merz “rule” constitutes another means to study chain-stretching effects present in a given flow system. Following a suggestion of Mead *et al.* in Ref. [24], we have compared the measured generalized extensional viscosity, η , for the steady-state flow generated in a two-roll mill as a function of the measured velocity-gradient (or “shear-rate”) $\dot{\gamma}$ for the entangled solutions with the corresponding dynamic linear viscoelastic measurement, i.e., $|\eta^*(\omega)|$, in the form of “Cox-Merz plots” shown in Figs. 29, 30, and 31. Both parameters are scaled with the zero-shear viscosity η_0 (see, Table I). The match between the

two sets of data at low deformation rates for all samples and that the values for these parameters are in the same ballpark provides an increased confidence on the choice of the corresponding η_0 values. At low and intermediate range of flow deformations, the values of these two sets of parameters are in a closer agreement for the samples with $N_e \sim 13$ than that for PS82 ($N_e \sim 7$). Apart from this, the overall dissimilarities between the deformation rate dependence of these two sets of results is obvious from these plots. At high deformation rates, chain-stretching effects become important, and, though it is not as strong as demanded by the DEMG model seen in Figs. 29, 30, and 31 in the previous section, its effect is strong enough to show an increased departure of η from the Cox-Merz superposition. This departure is quite expected, as we have noted above, since the chain-stretching effects are not accounted for in this empirical rule. The departure seen in the intermediate range of deformation rates is because of the fact that even in this regime, the flow experienced by the polymers in the stagnation region of a two-roll mill is very different from a shear-flow. In short, these figures provide a quantitative picture of the relative importance of chain-stretching to orientation effects.

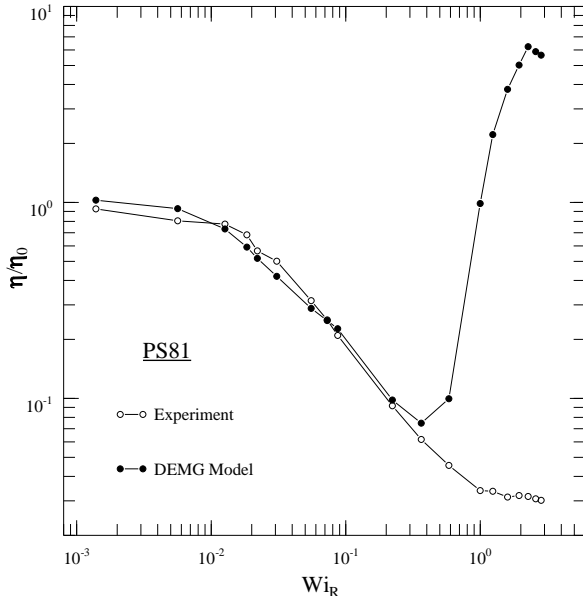


FIG. 29. The measured steady-state generalized extensional viscosity for the PS81 solution scaled with the zero-shear viscosity at several different Wi_R is compared with that computed from the DEMG model. The experimental results were obtained from the measured values of Δn , χ , $\dot{\gamma}$, λ , η_0 , and using the stress-optical relationship and the definition of η . The theoretical values were obtained from the computed values of Δn , χ and η_0 using the DEMG model with the measured values of $\dot{\gamma}$ and λ as input. The model parameters were $N_e = 13$, $n_t = 8420$, and $\tau_R = 2.25$ s.

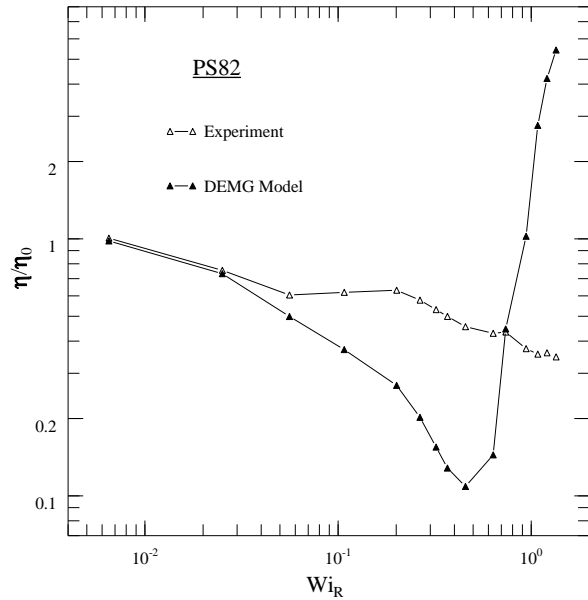


FIG. 30. A comparison of the experimental steady-state scaled generalized extensional viscosity η/η_0 versus Wi_R for the PS82 fluid (obtained from the measured values of Δn , χ , $\dot{\gamma}$, λ , η_0 , and with the use of the stress-optical relationship and the definition of η), with the predicted values obtained from the computed Δn , χ and η_0 , by using the DEMG model ($N_e = 7$, $n_t = 8420$, and $\tau_R = 3.01$ s.) with the measured $\dot{\gamma}$ and λ as input.

IV. SUMMARY AND CONCLUSIONS

The recently developed [7] dynamic light scattering section of the two-color flow birefringence experimental setup is used to characterize the steady-state flow-fields for a Newtonian fluid as well as for viscoelastic, entangled polymeric fluids in a two-roll mill, by measuring the velocity-gradient and the flow-type parameter for these fluids. Assuming Newtonian, creeping flow symmetry of the flow-field, the flow parameters for a Newtonian fluid, obtained directly from the decay rate of the autocorrelation functions measured at the stagnation region of the flow, are shown to be very well described by the Frazer's creeping flow solution [9].

The measured flow parameters for the polymeric fluids show clear departures from their corresponding Newtonian values, providing direct evidence of flow modification due to the conformational dynamics of the polymer molecules. Our results suggest that this departure may have a stronger dependence on the entanglement density of the polymer chains than on the molecular weight and concentration.

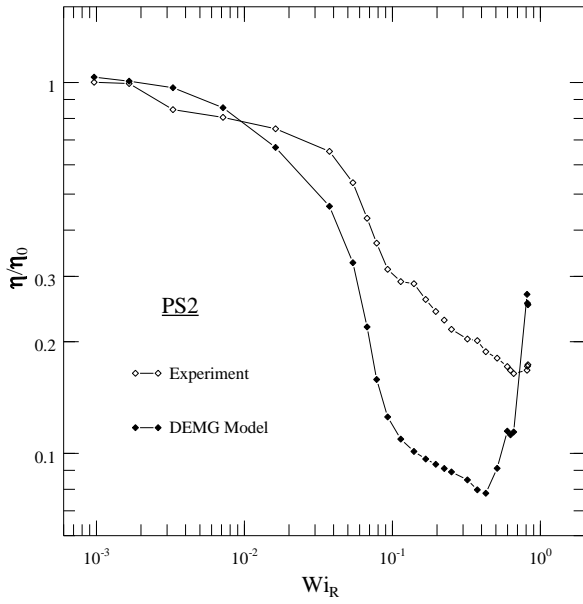


FIG. 31. A comparison of the steady-state generalized extensional viscosity for the PS2 solution scaled with zero-shear viscosity versus Wi_R , and that computed from the DEMG model. The experimental results were obtained from the measured values of Δn , χ , $\dot{\gamma}$, λ , η_0 , and by using the stress-optical relationship and the definition of η . The theoretical values were obtained from the computed values of Δn , χ and η_0 , by using the DEMG model with the measured $\dot{\gamma}$ and λ as input. The model parameters used were $N_e = 13$, $n_t = 2890$, and $\tau_R = 0.56$ s.

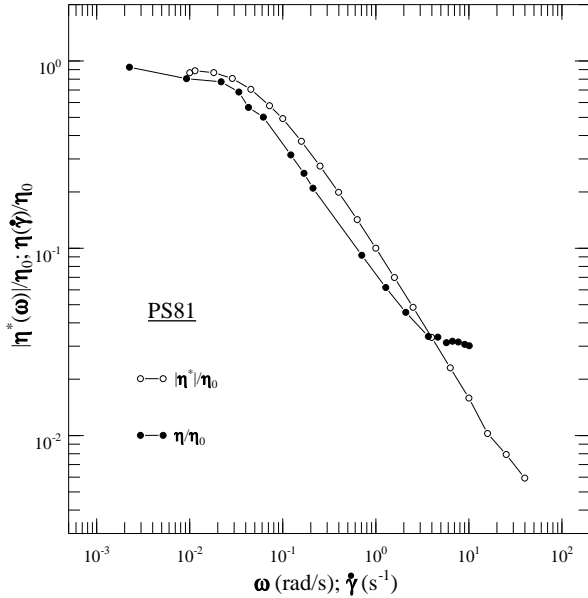


FIG. 32. The modulus of the complex viscosity, $|\eta^*|$, versus the angular frequency, ω (in rad/s), for the polystyrene solution PS81 is compared with the steady-state generalized extensional viscosity, η , versus the measured velocity-gradient, $\dot{\gamma}$ (in s^{-1}): the “Cox-Merz plot”. Both results are scaled by the measured zero-shear viscosity.

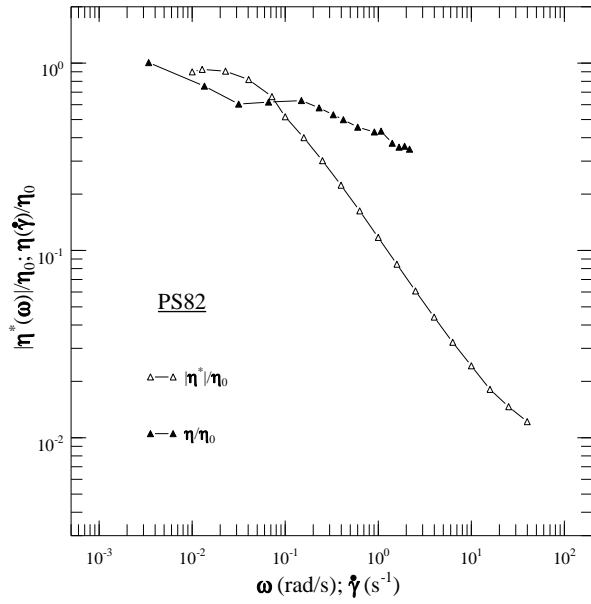


FIG. 33. A comparison of $|\eta^*|$ and η for the sample PS82 plotted against the radial frequency, ω (in rad/s), and the measured velocity-gradient, $\dot{\gamma}$ (in s^{-1}), respectively: the “Cox-Merz plot”. Both results are scaled by the measured zero-shear viscosity.

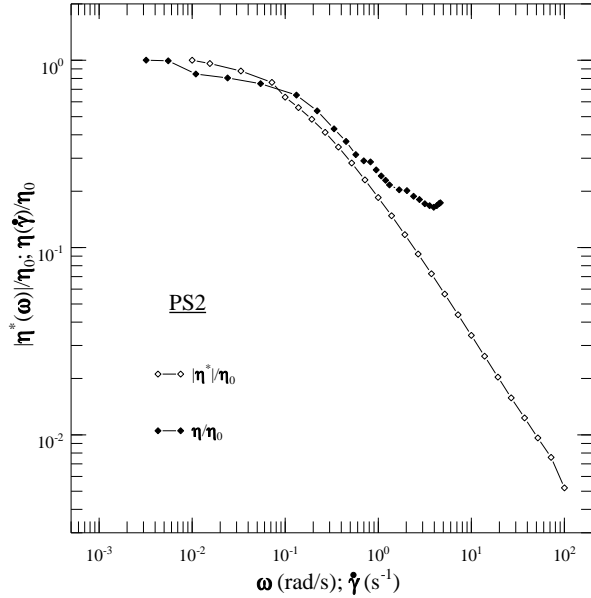


FIG. 34. The “Cox-Merz plot” for the polystyrene PS2 fluid, i.e., a combined plot of the scaled modulus of the complex viscosity, $|\eta^*|/\eta_0$, versus the angular frequency, ω (in rad/s), and the scaled steady-state generalized extensional viscosity, η/η_0 , versus the measured velocity-gradient, $\dot{\gamma}$ (in s^{-1}).

Within the limit of experimental error, the flow-field at the stagnation region of the two-roller is verified to retain its symmetry, for all rates of deformation studied with the Newtonian fluid and for the strain-rates $\dot{\gamma}_N \sqrt{\lambda_N} < 0.5$ s^{-1} ($Wi_R < 1$) with the polystyrene samples. The

flow-type parameter for the polystyrene fluids, extracted from the steady-state DLS experiments, was found to exceed its Newtonian value at very low rates of deformation. This result was verified to be consistent from three different experimental means.

The dynamics of the entangled polymers under study was coupled with the changes in the flow-field. As we have noted above, the DLS experiments has probed the effect of the viscoelasticity on the velocity field compared to its Newtonian form. On the other hand, the polymer response induced by the flow-fields generated by a two-roll mill is studied using two-color flow birefringence experiments, which were in turn compared with the birefringence predictions from the DEMG model using the measured flow data as input to the model.

Similar to the model predictions, the experimental birefringence results clearly illustrate the existence of three steady-state flow regimes. In the first two regimes of low and moderate rates of deformation, where the dynamics is dominated by chain segment re-orientation and reptational diffusion, the model predictions are qualitatively, and some times, quantitatively, reproduced in the experiments. However, the model is clearly inadequate in describing the polymer dynamics at sufficiently high rates of deformation, where chain-stretching is important. Our data do show signatures of chain-stretching: the experimental birefringence exceeds the plateau value, the Weissenberg number scaling behavior shown at the onset of chain-stretching by at least two of the three polymer samples studied, and the departure of the generalized extensional viscosity data from the empirical “Cox-Merz superposition”. The comparisons of the experimental birefringence as well as the generalized extensional viscosity data unambiguously indicates that the DEMG model overpredicts chain-stretching in these entangled samples. The relative values of birefringence, orientation angle, and viscosity for different entangled polymeric samples are shown to be determined by the competition between the effects of the corresponding flow-type parameter, molecular weight (via n_t) and the number entanglements per chain. Our experiments have demonstrated that the effect of N_e on these parameters is much stronger than that of the M_w and λ . We note that the model fails in describing the “smearing” of the expected plateau region in the birefringence curves. In particular, it overpredicts the tendency of the flow to rotate the polymer chains toward the outflow axis, at high Weissenberg numbers, thereby predicting excessive thinning of the generalized viscosity in this regime of flow for at least two of the polystyrene samples of our study. It was suggested in an earlier paper [12] that one of the prime causes for these deficiencies may be the fact that a real system experiences a conformation dependent decrease in the entanglement density (or a dilation in the tube diameter) as well as convective constraint-release, causing a decrease in the time scale for reptation with increasing flow strength that is not

included in the present form of the DEMG model. This calls for further efforts to improve reptation based constitutive models to obtain a better match of its predictions to experiments on entangled polymeric systems.

ACKNOWLEDGMENTS

We thank Johan Remmelgas for helpful discussions, critical reading of the manuscript and his help in the flow-symmetry calculation. We acknowledge James P. Oberhauser for the help with the DEMG model numerical simulation code.

-
- † Author for correspondence. Present address: Department of Physics and Astronomy, University of Pennsylvania, Philadelphia, PA 19104-6396, U.S.A. Electronic address: subrata@dept.physics.upenn.edu.
 - * Present address: Kimberly-Clark Co., Neenah, WI, U.S.A.
 - [1] G. Astarita, *J. Non-Newtonian Fluid Mech.* **6**, 69 (1979); W. L. Olbricht, J. M. Rallison and L. G. Leal, *J. Non-Newtonian Fluid Mech.* **10**, 291 (1982); R. I. Tanner, *AIChE J.* **22**, 910 (1976).
 - [2] N. S. Berman and J. W. Dunning, *J. Fluid Mech.* **61**, 289 (1973); R. V. Edwards, J. C. Angus, M. J. French and J. W. Dunning, *J. Appl. Phys.* **42**, 837 (1971).
 - [3] J. L. Balint, P. Vukoslavcevic, and J. M. Wallace, *A Study of the Vortical Structure of a Turbulent Boundary Layer*, (Springer-Verlag, New York, 1987), p. 456.
 - [4] M. Cloitre and E. Guyon, *J. Fluid Mech.* **164**, 217 (1986).
 - [5] J. C. A. Garcia and L. Hesselink, *Phys. Fluids A* **2**, 688 (1990).
 - [6] G. G. Fuller, J. M. Rallison, R. L. Schmidt, and L. G. Leal, *J. Fluid Mech.* **100**, 555 (1980).
 - [7] J. J. Wang, D. Yavich and L. G. Leal, *Phys. Fluids* **6**, 3519 (1994).
 - [8] H. Janeschitz-Kreigl, *Polymer Melt Rheology and Flow Birefringence*, (Springer-Verlag, New York, 1983).
 - [9] P. N. Dunlap and L. G. Leal, *J. Non-Newtonian Fluid Mech.* **23**, 5 (1987).
 - [10] E. Geffroy and L. G. Leal, *J. Non-Newtonian Fluid Mech.* **35**, 361 (1990); *J. Polym. Sci.: Polym. Phys. Ed.* **30**, 1329 (1992); E. Geffroy, Ph. D. Thesis, California Institute of Technology, U.S.A., 1991 (unpublished).
 - [11] D. S. Pearson, A. D. Kiss, L. J. Fetters and M. Doi, *J. Rheol.* **33**, 517 (1989).
 - [12] D. Yavich, D. W. Mead, J. P. Oberhauser and L. G. Leal, *J. Rheol.* **42**, 671 (1998).
 - [13] J. P. Oberhauser, L. G. Leal and D. W. Mead, *J. Polym. Sci. Polym. Phys. Ed.* **36**, 265 (1998).
 - [14] A. W. Chow and G. G. Fuller, *J. Rheol.* **28**, 23 (1984); G. G. Fuller, *Optical Rheometry of Complex fluids*, (Oxford University Press, Oxford, 1995).

- [15] P. L. Frattini and G. G. Fuller, *J. Rheol.* **28**, 61 (1984).
- [16] P. G. de Gennes, *J. Chem. Phys.* **55**, 572 (1971).
- [17] M. Doi and S. F. Edwards, *The Theory of Polymer Dynamics*, (Oxford U.P., New York, 1986).
- [18] A. J. Muller, J. A. Odell and A. Keller, *J. Non-Newtonian Fluid Mech.* **30**, 99 (1988); T. Q. Nguyen, G. Yu and H. -H. Kausch, *Macromolecules* **28**, 4851 (1995).
- [19] H. C. Booij and J. H. M. Palmen, *J. Non-Newtonian Fluid Mech.* **23**, 189 (1987); M. H. Wagner and J. Schaeffer, *Rheol. Acta* **31**, 22 (1992).
- [20] G. Marrucci and N. Grizzuti, *Gazzetta Chimica Italiana* **118**, 179 (1988).
- [21] D. S. Pearson, E. Herbolzheimer, N. Grizzuti and G. Marrucci, *J. Polym. Sci. Polym. Phys. Ed.* **29**, 1589 (1991).
- [22] D. W. Mead, E. A. Herbolzheimer and L. G. Leal, in *Theoretical and Applied Rheology*, Proceedings of the XIth International Congress on Rheology, edited by P. Moldenaers, and R. Keunings (Brussels, Belgium, 1992).
- [23] D. W. Mead and L. G. Leal, *Rheol. Acta* **34**, 339 (1995);
- [24] D. W. Mead, D. Yavich and L. G. Leal, *Rheol. Acta* **34**, 360 (1995).
- [25] K. Osaki, Y. Nishimura and M. Kurata, *Macromolecules* **18**, 1153 (1985).
- [26] J. D. Ferry, *Viscoelastic Properties of Polymers*, 2nd edition, (Wiley, New York, 1970).
- [27] E. V. Menezes and W. W. Graessley, *J. Polym. Sci. Polym. Phys. Ed.* **20**, 1817 (1982).
- [28] B. J. Berne and R. Pecora, *Dynamic Light Scattering*, (Wiley, New York, 1976).
- [29] S. Sanyal (unpublished).
- [30] W. H. Press, B. P. Flannery, S. A. Teukolsky and W. T. Vetterling, *Numerical Recipes, The Art of Scientific Computing*, (Cambridge University Press, New York, 1990).
- [31] S. Sanyal, D. Yavich and L. G. Leal, manuscript in preparation, 2000.
- [32] P. J. Flory, *Statistical Mechanics of Long Chain Molecules*, (Wiley Interscience, 1969).
- [33] V. Tirtaatmadja and T. Sridhar, *J. Rheol.* **39**, 1133 (1995); D. F. Jones and T. Sridhar, *ibid*, 713 (1995).
- [34] K. Wisbrun, *J. Rheol.* **30**, 1143 (1986).

TABLE I. The characteristic parameters for the three polystyrene samples.

Sample	M_w ($\times 10^6$)	c ($\frac{g}{cc}$)	η_0 (P)	N_e	τ_R (s)	n_t	K [P ($\frac{rad}{s}$) n]	n
PS81	8.42	0.0396	7500	~ 13	2.25	8420	343.72	-0.80
PS82	8.42	0.0262	2700	~ 7	3.01	8420	190.11	-0.70
PS2	2.89	0.0867	19000	~ 13	0.56	2890	2703.96	-0.83

TABLE II. The characteristic parameters for the two-roll mill with radius R , height H , and gap G .

Roller	R (cm)	G (cm)	$\frac{H}{G}$	$(\frac{\dot{\gamma}N}{\omega})_{th}$	$(\frac{\dot{\gamma}N}{\omega})_{exp}$	$(\lambda N)_{th}$	$(\lambda N)_{exp}$
G	1.278	0.844	3.1	2.7	2.8	1.501	0.1508

TABLE III. The values of the parameter $h(\phi)$ for three orientations ϕ of the two-roll mill and that for the special case of a symmetric flow ($\epsilon = 0$).

ϕ	General	Symmetric flow
0°	$\dot{\gamma}^2 + \epsilon^2$	$\dot{\gamma}^2$
90°	$\dot{\gamma}^2 \lambda^2 + \epsilon^2$	$\dot{\gamma}^2 \lambda^2$
45°	$\epsilon^2 + \frac{1}{2}\dot{\gamma}^2(1 + \lambda^2) + \epsilon\dot{\gamma}(1 - \lambda)$	$\frac{1}{2}\dot{\gamma}^2(1 + \lambda^2)$